Monthly Notices of the ROYAL ASTRONOMICAL SOCIETY

MNRAS **520,** 3669–3687 (2023)
Advance Access publication 2023 January 30

https://doi.org/10.1093/mnras/stad307

The SCUBA-2 Large eXtragalactic Survey: 850 μm map, catalogue and the bright-end number counts of the *XMM*-LSS field

T. K. Garratt [1★] J. E. Geach [1] Y. Tamura [2] K. E. K. Coppin [1] M. Franco,[1] Y. Ao,[3,4] C. -C. Chen [5] C. Cheng,[6] D. L. Clements [7] Y. S. Dai,[6,8] H. Dannerbauer,[9,10] T. R. Greve,[11,12] B. Hatsukade [13] H. S. Hwang,[14,15] L. Jiang,[16] K. Kohno [13] M. P. Koprowski,[17] M. J. Michałowski [18] M. Sawicki,[19] D. Scott,[20] H. Shim,[21] T. T. Takeuchi [2,22] W. -H. Wang,[5] Y. Q. Xue[4,23] and C. Yang [24]

Affiliations are listed at the end of the paper

Accepted 2023 January 25. Received 2023 January 24; in original form 2022 November 29

ABSTRACT

We present 850 μm imaging of the *XMM*-LSS field observed for 170 h as part of the James Clerk Maxwell Telescope SCUBA-2 Large eXtragalactic Survey (S2LXS). S2LXS *XMM*-LSS maps an area of 9 deg^2, reaching a moderate depth of $1\sigma \simeq 4\,\mathrm{mJy\,beam^{-1}}$. This is the largest contiguous area of extragalactic sky mapped by James Clerk Maxwell Telescope (JCMT) at 850 μm to date. The wide area of the S2LXS *XMM*-LSS survey allows us to probe the ultra-bright ($S_{850\mu\mathrm{m}} \gtrsim 15$ mJy), yet rare submillimetre population. We present the S2LXS *XMM*-LSS catalogue, which comprises 40 sources detected at $>5\sigma$ significance, with deboosted flux densities in the range of 7–48 mJy. We robustly measure the bright-end of the 850 μm number counts at flux densities >7 mJy, reducing the Poisson errors compared to existing measurements. The S2LXS *XMM*-LSS observed number counts show the characteristic upturn at bright fluxes, expected to be motivated by local sources of submillimetre emission and high-redshift strongly lensed galaxies. We find that the observed 850 μm number counts are best reproduced by model predictions that include either strong lensing or source blending from a 15-arcsec beam, indicating that both may make an important contribution to the observed overabundance of bright single dish 850 μm selected sources. We make the S2LXS *XMM*-LSS 850 μm map and $>5\sigma$ catalogue presented here publicly available.

Key words: catalogues – surveys – galaxies: high-redshift – submillimetre: galaxies.

1 INTRODUCTION

Historically our knowledge of how galaxies form and evolve has been driven by observations made at optical wavelengths. However, over the past 50 yr, helped by the boom in infrared/millimetre facilities (both ground based and in space), the study of the Universe at infrared/millimetre wavelengths has quickly gained momentum. The first infrared observations targeted a small number of known extragalactic sources revealing that some galaxies emit the same amount of energy in the infrared as at optical wavelengths (e.g. Low & Kleinmann 1968; Kleinmann & Low 1970). Over the course of the following decade the scale of infrared surveys dramatically expanded, with the first all-sky infrared survey (the *Infrared Astronomical Satellite* mission; Neugebauer et al. 1984) detecting ∼20 000 local starburst galaxies, the majority of which were too faint to be included in previous optical catalogues (Beichman et al. 1988). In the 1990's, the NASA *Cosmic Background Explorer* (Boggess et al. 1992) gave us the first measurements of the cosmic infrared background (CIB; the integrated infrared emission from all galaxies in the history of the Universe). These data (e.g. Puget et al. 1996; Fixsen et al. 1998; Hauser et al. 1998), along with measurements of the CIB at mid-infrared wavelengths (e.g. Papovich et al. 2004; Dole et al. 2006) revealed that the extragalactic background light has comparable intensities at optical ($\lambda < 8$ μm) and infrared ($\lambda > 8$ μm) wavelengths, meaning that around half the optical and ultraviolet emission from galaxies is absorbed by interstellar dust and re-emitted in the far-infrared (e.g. Hauser & Dwek 2001; Dole et al. 2006).

The most luminous infrared galaxies are known as ultra luminous infrared galaxies (ULIRGs) and hyper luminous infrared galaxies (HyLIRGs) with integrated infrared luminosities of $L_{\mathrm{IR}} > 10^{12}$ and $L_{\mathrm{IR}} > 10^{13}\,\mathrm{L_\odot}$, respectively, and star formation rates commonly in excess of $50\,\mathrm{M_\odot\,yr^{-1}}$ (e.g. Sanders & Mirabel 1996; Casey, Narayanan & Cooray 2014). In these dusty star-forming galaxies light from young, short-lived, massive stars is absorbed by the surrounding dust and re-radiated at infrared wavelengths.

Dusty star-forming galaxies detected at submillimetre wavelengths are commonly known as submillimetre galaxies (SMGs). Since the first observations of SMGs in the late 1990's (e.g. Smail, Ivison & Blain 1997; Barger et al. 1998; Hughes et al. 1998) there has been considerable progress in our understanding of their physical properties and cosmological significance in the context of galaxy evolution (see Casey et al. 2014; Hodge & da Cunha 2020, for detailed reviews). We now know that SMGs selected at 850 μm are intrinsically highly infrared luminous ($L_{\mathrm{IR}} > 10^{12}\,\mathrm{L_\odot}$) with star formation rates in excess of $100\,\mathrm{M_\odot\,yr^{-1}}$ (e.g. Chapman et al.

★ E-mail: t.garratt@herts.ac.uk

© The Author(s) 2023.
Published by Oxford University Press on behalf of Royal Astronomical Society. This is an Open Access article distributed under the terms of the Creative Commons Attribution License (https://creativecommons.org/licenses/by/4.0/), which permits unrestricted reuse, distribution, and reproduction in any medium, provided the original work is properly cited.

Downloaded from academic.oup.com/mnras/article/520/3/3669/7009221 by guest on 23 October 2026

2005; Magnelli et al. 2012; Swinbank et al. 2014; Ikarashi et al. 2015; Michałowski et al. 2017; Miettinen et al. 2017), have a number density which peaks at $\langle z \rangle \approx 2$–3 (e.g. Chapman et al. 2005; Pope et al. 2005; Wardlow et al. 2011; Simpson et al. 2014; Chen et al. 2016; Miettinen et al. 2017), have high stellar masses ($M_* > 10^{10}\,\mathrm{M}_\odot$; e.g. Swinbank et al. 2004; Hainline et al. 2011; Michałowski et al. 2012; da Cunha et al. 2015; Michałowski et al. 2017), are gas-rich (e.g. Frayer et al. 1998; Greve et al. 2005; Tacconi et al. 2006; Ivison et al. 2011; Thomson et al. 2012; Bothwell et al. 2013), often host active galactic nuclei (e.g. Alexander et al. 2005; Pope et al. 2008; Johnson et al. 2013; Wang et al. 2013), and with a volume density three orders of magnitude greater than that of local ULIRGS (e.g. Smail et al. 1997; Chapman et al. 2005) contribute approximately 20 per cent of the total star formation rate density over a redshift range 1–4 (e.g. Casey et al. 2013; Swinbank et al. 2014). These properties make SMGs excellent candidates for the progenitor population of massive elliptical galaxies seen in the local Universe today.

Submillimetre astronomy benefits from a strong negative K correction that arises from the shape of the intrinsic spectral energy distribution (SED) of a typical star-forming galaxy, which peaks at 100 μm. When we observe emission from a local star-forming galaxy at a wavelength of 850 μm we are probing the Rayleigh–Jean's tail (the rest-frame cold dust continuum emission) of the galaxy's intrinsic SED, and so, as we observe star-forming galaxies at increasing cosmological distances the rest-frame emission we observe at 850 μm moves up the Rayleigh–Jeans tail, closer to the peak of the intrinsic SED. The increasing power of rest-frame emission with increasing cosmological distance compensates for cosmological dimming. This means that submillimetre galaxies of equal luminosity that lie at $1 < z < 8$ will have similar observed fluxes at 850 μm, making SMGs a useful probe of the early Universe.

The first extragalactic submillimetre surveys were conducted with the Submillimeter Common User Bolometer Array camera (SCUBA; Holland et al. 1999) mounted on the James Clerk Maxwell telescope (JCMT), providing the first census of dust-obscured star formation in distant galaxies at submillimetre wavelengths (Smail et al. 1997; Barger et al. 1998; Hughes et al. 1998). Subsequent extragalactic submillimetre surveys built on the success of these early observations, and aided by the development of new submillimetre/millimetre instruments such as the Large Apex BOlometer Camera Array (LABOCA; Siringo et al. 2009), AzTEC (Wilson et al. 2008), and the MAx-Planck Millimeter BOlometer (MAMBO; Kreysa et al. 1998), the scale of extragalactic surveys at submillimetre/millimetre wavelengths expanded (e.g. Eales et al. 2000; Coppin et al. 2006; Scott et al. 2008; Weiß et al. 2009). However, the limited field of view and sensitivity of the early submillimetre/millimetre instruments made it difficult to map large areas of the sky (i.e. $> 1\,\mathrm{deg}^2$), with the largest and deepest of these surveys detecting around 100 sources (Coppin et al. 2006; Weiß et al. 2009), insufficient numbers for robust statistical studies of this cosmologically important population of galaxies.

A breakthrough in single-dish submillimetre astronomy came with the introduction of SCUBA-2 (Holland et al. 2013), the second-generation bolometer array on the JCMT. SCUBA-2 is a dual wavelength camera with two arrays of 5120 pixels that simultaneously map the sky at wavelengths of 450 and 850 μm, covering a field of view of $8\,\mathrm{arcmin}^2$. With a mapping speed that is over an order of magnitude faster than that of its predecessor (at equivalent depth), SCUBA-2 opened the door for wide area (i.e. $> 1\,\mathrm{deg}^2$) surveys at submillimetre wavelengths. The first such survey was the SCUBA-2 Cosmology Legacy Survey (S2CLS; Geach et al. 2017), which began shortly after the commissioning of SCUBA-2. This survey, the largest of seven JCMT Legacy Survey programs, mapped a total area of $5\,\mathrm{deg}^2$ over seven extragalactic fields to a median depth (at 850 μm) of $1\sigma \simeq 1\,\mathrm{mJy\,beam}^{-1}$. Owing to the wide-area and depth of S2CLS, this survey detected almost 3000 sources at a significance of $>3.5\sigma$ in the 850 μm maps, a sample an order of magnitude larger than in previous submillimetre surveys, allowing the single dish 850 μm number counts to be measured to unprecedented accuracy. The S2CLS 850 μm number counts are well fit by a Schechter (1976) function of the form

$$\frac{\mathrm{d}N}{\mathrm{d}S} = \left(\frac{N_0}{S_0}\right)\left(\frac{S}{S_0}\right)^{-\gamma} \exp\left(-\frac{S}{S_0}\right), \quad (1)$$

with $N_0 = 7180 \pm 1200\,\mathrm{deg}^{-2}$, $S_0 = 2.5 \pm 0.4\,\mathrm{mJy\,beam}^{-1}$, and $\gamma = 1.5 \pm 0.4$. However, at intrinsic fluxes above 15 mJy there is a clear upturn in the S2CLS source counts, which lie above the Schechter (1976) function fit. An overabundance of bright sources is also seen at far-infrared wavelengths in the *Herschel* Astrophysical Terahertz Large Area Survey (H-ATLAS; Eales et al. 2010; Negrello et al. 2010) and the *Herschel* Multi-tiered Extragalactic Survey (HerMES; Oliver et al. 2012; Wardlow et al. 2013), and at millimetre wavelengths (but only at high flux densities, $S_{1.4\,\mathrm{mm}} \gtrsim 10\,\mathrm{mJy}$, corresponding to $S_{850\,\mu\mathrm{m}} \gtrsim 40\,\mathrm{mJy}$) in the South Pole Telescope Sunyaev–Zel'dovich survey (SPT–SZ; Vieira et al. 2010; Mocanu et al. 2013), and is attributed to the presence of local objects and high-redshift gravitationally lensed sources. It has been demonstrated that a simple flux density cut at 100 mJy in the *Herschel* 500 μm band is almost 100 per cent effective at selecting strongly lensed galaxies, after local ($z < 0.1$) sources of emission have been removed (Negrello et al. 2010; Wardlow et al. 2013). S2CLS (Geach et al. 2017) provides tentative evidence that a flux cut at 850 μm may yield a similar result – the brightest 850 μm selected sources in this survey are a lensed high-redshift galaxy ('Orochi'; Ikarashi et al. 2011) and a well-known Galactic object (the Cat's Eye Nebula). However, with only six 850 μm selected sources in S2CLS with intrinsic fluxes above 15 mJy, the bright end of the number counts remains poorly constrained and the potential of a flux cut at this wavelength to select strongly lensed galaxies barely explored. The brightest submillimetre galaxies selected at 850 μm are also observed to be the most distant (e.g. Stach et al. 2019; Simpson et al. 2020; Chen et al. 2022), but with so few single dish selected 850 μm sources with flux densities $S_{850\,\mu\mathrm{m}} > 15\,\mathrm{mJy}$ the redshift distribution of sources in this flux regime is poorly constrained, and the trend of increasing redshift with submillimetre flux density is untested for these ultrabright sources. Intrinsically bright submillimetre sources are rare, with abundances for sources with flux densities >20 mJy currently estimated to be only ≈0.5–5 galaxies per square degree (e.g. Béthermin et al. 2012; Geach et al. 2017), and so a moderate depth survey at 850 μm with an area $> 10\,\mathrm{deg}^2$ is needed to properly probe this far-infrared luminous, and potentially high-redshift population of galaxies.

The SCUBA-2 Large eXtragalactic Survey (S2LXS) is a JCMT Large Program (PI: J. E. Geach and Y. Tamura) and covers an area of $10\,\mathrm{deg}^2$ split over two fields – the X-ray Multi-Mirror Large-Scale Structure Survey field (*XMM*-LSS; Pierre et al. 2004) and the Extended Cosmic Evolution Survey field (E-COSMOS; Scoville et al. 2007). In the context of other JCMT Large Programs S2LXS can be seen as a wide, moderately deep tier, complementing the SCUBA-2 Cosmology Legacy Survey (S2CLS; Geach et al. 2017), the SCUBA-2 COSMOS survey (S2COSMOS; Simpson et al. 2019), and the SCUBA-2 Ultra Deep Imaging East Asian

Downloaded from academic.oup.com/mnras/article/520/3/3669/7009221 by guest on 23 October 2026

Table 1. Summary of ancillary multiwavelength data for the S2LXS *XMM*-LSS field. Note that a region of this field (central coordinates $\alpha = 34.^{\circ}4542$, $\delta = -5.^{\circ}0986$) was observed at 850 μm in S2CLS (Geach et al. 2017). Observations of this region are not repeated in S2LXS.

Survey/instrument	Abbreviation	Band	Reference
X-ray Multi-Mirror Large Scale Structure Survey	*XMM*-LSS	(0.5–2) keV	Pierre et al. (2004)
X-ray Multi-Mirror *Spitzer* Extragalactic Representative Volume Survey	*XMM*-SERVS	(0.5–10) keV	Chen et al. (2018)
Canada–France–Hawaii Telescope Large Area *U*-band Deep Survey	CFHT CLAUDS	u^*	Sawicki et al. (2019)
Hyper Suprime-Cam Subaru Strategic Program	HSC-SSP	*grizy*	Aihara et al. (2018)
Visible and Infrared Survey Telescope for Astronomy Deep Extragalactic Observations survey	VISTA VIDEO	*YJHK*	Jarvis et al. (2013)
United Kingdom infrared telescope Infrared Deep Sky Survey Deep eXtragalactic Survey	UKIDSS DXS	*YJHK*	Lawrence et al. (2007)
Spitzer Extragalactic Representative Volume Survey	SERVS	3.6 μm, 4.5 μm	Mauduit et al. (2012)
Spitzer survey of the Deep Drilling Fields	Deep Drill	3.6 μm, 4.5 μm	Lacy et al. (2021)
Spitzer Wide-area InfraRed Extragalactic survey	SWIRE	3.6 μm, 4.5 μm, 5.8 μm, 8.0 μm, 24 μm, 70 μm, 160 μm	Lonsdale et al. (2003)
Herschel Multi-tiered Extragalactic Survey	HerMES	250 μm, 350 μm, 500 μm	Oliver et al. (2012)
LOw Frequency ARray	LOFAR	120–168 MHz	Hale et al. (2019)
MeerKAT International GigaHertz Tiered Extragalactic Explorations	MIGHTEE	856–1712 MHz	Heywood et al. (2022), Jarvis et al. (2016)
Very Large Array 1–2 GHz survey	–	1–2 GHz	Heywood et al. (2020)
SCUBA-2 Cosmology Legacy Survey	S2CLS	450 μm, 850 μm	Geach et al. (2017)

Observatory Survey (STUDIES; Wang et al. 2017), which map smaller areas to higher sensitivity. S2LXS covers an area 2 × larger than S2CLS, is effectively 2 × deeper than SPT–SZ (Vieira et al. 2010; Mocanu et al. 2013) and at a wavelength of 850 μm is more sensitive to dust emission from high redshift ($z \gtrsim 4$) SMGs than far-infrared surveys (i.e. H-ATLAS, HerMES; Eales et al. 2010; Oliver et al. 2012). The primary aims of S2LXS are to detect the most luminous and highest redshift submillimetre sources, thus providing robust constraints on the bright-end of the single-dish 850 μm number counts and unveiling a new distant population of SMGs.

In this paper, we present the results of the S2LXS *XMM*-LSS field and provide the map and source catalogue for public use. This paper is organized as follows: in Section 2, we define the survey and describe the data reduction; in Section 3, we present the maps and describe the cataloguing procedure; in Section 4, we use these data to measure the bright-end of the 850 μm number counts and compare to recent results from model predictions; and in Section 5 we summarize the paper.

2 THE SCUBA-2 LARGE EXTRAGALACTIC SURVEY

The SCUBA-2 Large eXtragalactic Survey (S2LXS) is a wide area (>10 deg^2) survey at 850 μm split over two fields: *XMM*-LSS (9 deg^2); and E-COSMOS (3 deg^2). These fields were selected to take advantage of the wealth of legacy multiwavelength data available (this data are essential for identifying SMG counterparts) and for the accessibility to key submillimetre/millimetre interferometers for follow-up observations. The S2LXS observations of the E-COSMOS field are currently less than 50 per cent complete and continue under programme ID M20AL026 (PI: J. E. Geach and Y. Tamura). The S2LXS map, catalogue and results for the E-COSMOS field will be the subject of a future paper. Therefore, the focus of this paper is the S2LXS *XMM*-LSS field, which is mapped at 850 μm to a median depth of $1\sigma \simeq 4$ mJy beam^{-1}. Although SCUBA-2 simultaneously collects data at both 850 and 450 μm we do not process the complementary 450 μm data. At 450 μm, the estimated sensitivity is $1\sigma \simeq 50$ mJy beam^{-1} and so these data are not expected to have sufficient depth to reliably detect (at $>3.5\sigma$) even the most luminous submillimetre sources in the S2LXS *XMM*-LSS field.

XMM-LSS benefits from being a well-studied deep field in the Hyper Suprime-Cam (HSC) Subaru Strategic Program (HSC-SSP). The HSC-SSP is multiband (*grizy*+narrow band) imaging survey (Aihara et al. 2018) conducted using the HSC digital imaging camera on the 8.2 m Subaru Telescope. This survey comprises three tiers; a wide tier (1400 deg^2, $r_{\rm AB} \simeq 26$), a deep tier (28 deg^2, $r_{\rm AB} \simeq 27$), and an ultradeep tier (13.5 deg^2, $r_{\rm AB} \simeq 28$). The *XMM*-LSS field is also covered by legacy data sets at X-ray, ultraviolet, infrared, and radio wavelengths (see Table 1 for a summary of the multiwavelength imaging available). Multiwavelength data is essential for identifying counterparts and companions (e.g. satellite galaxies that are not dusty) to sources detected at 850 μm.

2.1 Observations

The S2LXS *XMM*-LSS observations were conducted with SCUBA-2 (Holland et al. 2013) on the James Clerk Maxwell telescope (JCMT) over 3 yr from 2017 July to 2020 January, totalling 170 h. The *XMM*-LSS field was mapped using the SCUBA-2 PONG mapping strategy (Holland et al. 2013) for large fields in which the telescope array tracks across a target multiple times bouncing off the edges of a defined rectangular map area. Once the PONG pattern fills the map area the map is rotated and the pattern is repeated at the new angle. In Fig. 1, we show an example of the telescope track to illustrate the rotating PONG pattern. Observations were conducted for S2LXS *XMM*-LSS using the SCUBA-2 PONG 1800 arcsec diameter map pattern, which has a telescope scanning speed of 400 arcsec s^{-1} with 8 rotations of the map during each observation to ensure a uniform coverage of the field. The final S2LXS *XMM*-LSS field map is a mosaic of 42 hexagonally arranged 1800-arcsec diameter PONG tiles with each tile overlapping with its neighbours. We show the layout of the PONG tiles in Fig. 1. There is a gap in the observations centred on $\alpha = 34.^{\circ}4542$, $\delta = -5.^{\circ}0986$. This absence of data reflects the area of the deeper ($1\sigma = 1$ mJy beam^{-1}) S2CLS observations

Downloaded from academic.oup.com/mnras/article/520/3/3669/7009221 by guest on 23 October 2026

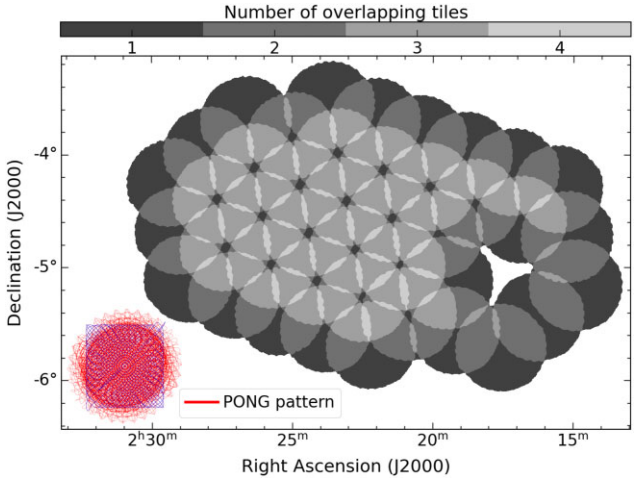


Figure 1. Layout of the S2LXS map showing the 42 hexagonally arranged PONG tiles. An exposure time crop is applied to each individual PONG tile (see Section 2.2 for details) before these are mosaicked. The colour map shows the number of PONG tiles that overlap across the map. The absence of data around $\alpha = 34.^{\circ}4542$, $\delta = -5.^{\circ}0986$ corresponds to the area of the deeper $1\sigma = 1$ mJy beam^{-1} S2CLS UKIDSS-UDS field observations (Geach et al. 2017). This region was not observed again in S2LXS. In the lower left of the figure, we also show an example of the telescope track for a PONG observation to illustrate the rotating PONG pattern (Holland et al. 2013). The blue line shows the telescope track for a single rotation of the map, and the red line shows the complete PONG pattern (i.e. 8 rotations of the map).

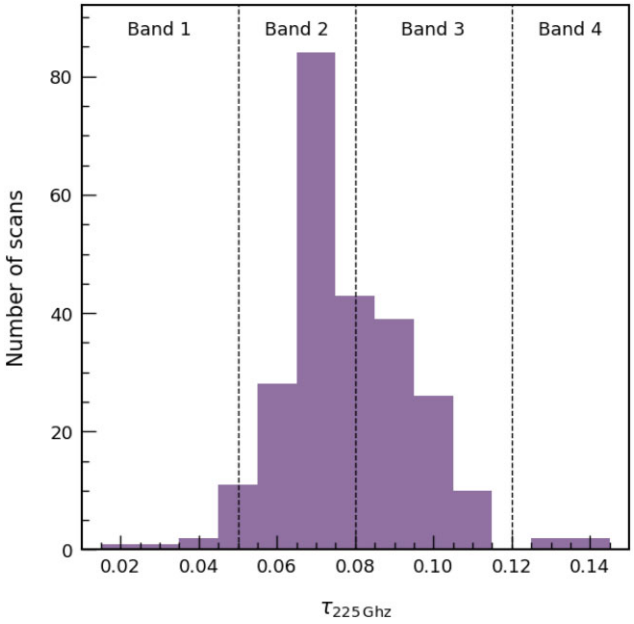


Figure 2. Zenith opacity at 225 GHz. The opacity is recorded at the beginning and end of each PONG scan. We show the distribution of the average of these measurements (i.e. $\tau_{225} = (\tau_{\rm start} + \tau_{\rm end})/2$). For clarity, we also show the boundaries of the JCMT weather bands.

of the UKIRT Infrared Deep Sky Survey-Ultra Deep Survey field (S2CLS UKIDSS-UDS; Geach et al. 2017). This region was not observed again in S2LXS *XMM*-LSS.

The original objective of S2LXS was to map the *XMM*-LSS field to a depth of $1\sigma \simeq 2$ mJy beam^{-1} at 850 μm. Progress of the survey was slow due to ongoing bad weather conditions on Mauna Kea and S2LXS *XMM*-LSS was consequently scaled back with the revised aim to map the S2LXS *XMM*-LSS field to a target sensitivity of $1\sigma \simeq 4$ mJy beam^{-1}. At this depth the primary objective of S2LXS, to uncover the intrinsically rare, bright-end of the SMG population, is still realised. The individual PONG observations were limited to an integration time of 40 min to allow for accurate monitoring of variations in the observing conditions with regular pointing observations being made throughout the night. Each of the 42 PONG tiles were observed over a minimum of 5 scans (a minimum combined observing time of 3 h) to achieve the target sensitivity of $1\sigma \simeq 4$ mJy beam^{-1}. The majority of observations (97 per cent) were conducted in band 1, 2, or 3 weather conditions (i.e. $\tau_{225\,\rm GHz} \leq 0.12$). The remaining 3 per cent of observations were taken in band 4 conditions in which the opacity at 225 GHz is in the range $0.12 < \tau_{225\,\rm GHz} < 0.16$ (see Fig. 2). In the following section, we describe the process used to produce the S2LXS *XMM*-LSS maps.

2.2 Data reduction

The SCUBA-2 bolometers each record a time-varying signal containing contributions from astronomical signal, atmospheric extinction, and noise. We reduce the S2LXS time-series data using the Dynamical Iterative Map-Maker (DIMM) tool, part of the Submillimetre Common User Reduction Facility software package (SMURF; Chapin et al. 2013). The primary purpose of this data reduction is to extract the astronomical signal from the SCUBA-2 bolometer time streams and to bin the resulting data into a 2D celestial projection. DIMM includes a specialised 'blank-field' configuration with parameters tuned for data reduction in extragalactic surveys. These parameters were optimized in the SCUBA-2 Cosmology Legacy Survey (S2CLS; Geach et al. 2017). Taking this optimized configuration as the starting point we run several test data reductions using the S2LXS *XMM*-LSS raw data, varying the DIMM parameters and analysing the output (the reduced data). Our aim is to find the combination of parameters that best reduce residual noise in the S2LXS *XMM*-LSS map without overly compromising the astronomical signal. For full details of DIMM see Chapin et al. (2013). Here, we provide a short description of the main stages of DIMM data reduction (illustrated in the flow chart in Fig. 3) and describe the specific parameters we use to reduce the S2LXS *XMM*-LSS data.

The first step in DIMM data reduction is the pre-processing stage in which the time-stream data are down-sampled and cleaned. The response of each bolometer to changing sky power is measured at the beginning and end of each observation (flat-field scans). In the pre-processing stage, the raw data are first multiplied by a flat-field correction (estimated using the flat-field scans) to calibrate the bolometers. The time-streams are then down-sampled to a rate that matches the pixel scale of the final map (2 arcsec). Next the time-stream data are cleaned for short-duration and high-amplitude spikes. In this step, the signal from bright point sources can be mistaken for high-amplitude noise spikes and erroneously excluded. To avoid this, we adopt a conservative threshold of 5σ and a box width of 50 time slices. At each time slice the median value of samples within a box centred on the time slice is measured. A time slice is flagged as a spike if the residual between the time slice value and this median value is greater than 5 × the local noise (the standard deviation of values in the neighbouring 'down-stream' box). Next any sudden steps in the time series are identified and removed. Gaps are filled using a linear interpolation of the 50 time slices preceding and the 50 time slices following the excluded data. An order 1 polynomial (i.e. linear) estimate of the base-line is then removed from each bolometer. In the final step of the DIMM

Downloaded from academic.oup.com/mnras/article/520/3/3669/7009221 by guest on 23 October 2026

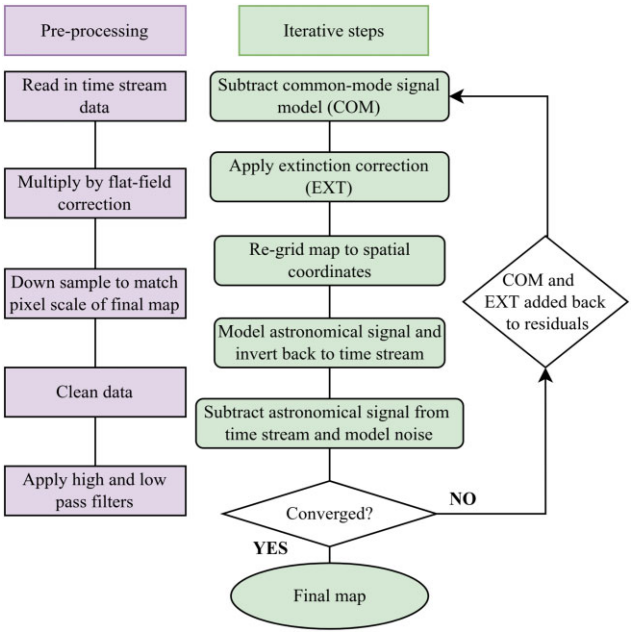


Figure 3. Flowchart illustrating the main stages of DIMM data reduction.

pre-processing stage each bolometer time stream is independently filtered. A high pass filter is used to remove frequencies that correspond to spatial scales of $\theta > 150$ arcsec (to suppress large-scale structures) and a low-pass filter used to exclude data corresponding to angular scales of $\theta < 2$ arcsec (so that the beam is fully sampled).

Next DIMM begins an iterative process. First the common-mode signal (the average signal seen by all bolometers) is independently modelled for each SCUBA-2 sub-array and subtracted from the cleaned time-stream data. A multiplicative extinction correction (derived from atmospheric opacity measurements from the JCMT water vapour monitor) is then applied. In the second and any subsequent iterations, the model of the astronomical signal estimated in the previous iteration is added back into the time series data at this stage. The next step is to model the astronomical signal. To do this the time series data are first binned onto a 2D celestial projection. Each pixel in this 2D grid is sampled many times by independent bolometers owing to the PONG scanning pattern and so, assuming that previous steps have removed all other sources of emission, the astronomical signal can be accurately estimated for a given pixel by taking the weighted average of the bolometer values that contribute to that pixel. The astronomical signal model is inverted back to the time stream and subtracted from the data, leaving just residual noise (made up of instrumental noise and atmospheric effects). This step in the iterative process can also be used to perform map-based despiking in which the scatter in the samples of a given map pixel is used to exclude outliers in the time-stream data. Since real astronomical sources have a fixed spatial location, bright point sources are unlikely to be falsely identified as spikes in this approach and so we can use a more stringent threshold here. Time-series residuals that differ by more than 3σ from the mean value in a map pixel are flagged and these are not used in following iterations. Finally a noise model is estimated for each bolometer by measuring the residual. This noise model is only estimated on the first iteration and is used to weight the data during the mapping process in subsequent iterations. This iterative process continues until either 20 iterations have completed or the normalized mean change between consecutive maps is less than 0.05. If further iterations are needed then all models (except the astronomical signal which is added back in later) are added back into the time-stream residuals.

To convert the map from units of pW to Jy beam^{-1} we apply a flux conversion factor (FCF) to the reduced map. We use the recently revised values for the standard FCF from Mairs et al. (2021), and for observations taken before 2018 June 30 we adopt the standard FCF value of 516 Jy beam^{-1} pW^{-1} and for observations taken after this date we use the standard FCF value of 495 Jy beam^{-1} pW^{-1}. We also apply an upwards correction of 10 per cent (estimated in S2CLS, see Geach et al. 2017) to account for the loss of flux density due to the filtering steps of the data reduction. The absolute flux calibration is estimated to be accurate to within 15 per cent (e.g. Geach et al. 2017).

Each of the approximately 40 min PONG observations (PONG scans) are reduced independently to produce a set of individual maps for each of the 42 PONG regions. We combine all scans for each PONG region using the PICARD package within SMURF and the recipe MOSAIC_JCMT_IMAGES. This recipe combines the maps using inverse-variance weighting with the variance of the final map calculated from the input variances. This gives us the 42 PONG tiles which will make up the final S2LXS *XMM*-LSS map.

The PONG mapping strategy provides uniform coverage within the PONG diameter (i.e. within a 1800-arcsec diameter). However, outside the PONG diameter (the overscan region) each map pixel in the PONG scan is sampled less frequently. As the map pixels are sparsely sampled at the edges of the overscan region the steps taken in the DIMM reduction to remove high amplitude spikes perform poorly. Consequently, at the edges of this overscan region we see a multitude of very high (low) value pixels. The paucity of the sampling also results in variance estimates which are not robust. This is problematic as a very high pixel value combined with an inaccurate variance estimate can masquerade as a bright point source in the outskirts of a PONG tile (see Fig. 4). To mitigate this, we apply an exposure time crop to the PONG tiles with the aim of eliminating these (obviously) spurious sources, whilst preserving as much of the data as possible. We iterate through increasingly stringent exposure time cuts until we find the minimum exposure time limit that effectively excludes these high (low) value pixels in the overscan regions. In Fig. 4, we highlight the optimum exposure time limit of 1.7 s.

We use the software package SWARP (Bertin et al. 2002) to individually resample the PONG tiles (using nearest neighbour interpolation) to match the astrometric projection and pixel grid of the final science map. The resampled PONG tiles are then combined using inverse variance weighting to produce a map of the S2LXS *XMM*-LSS field (see Fig. 1 for the layout of the PONG tiles).

To optimize the detection of point sources, we apply a matched filter to the final mosaic using the PICARD recipe SCUBA2_MATCHED_FILTER. Matched filtering consists of two stages. First, the S2LXS map is smoothed with a Gaussian of full-width-half-maximum (FWHM) 30 arcsec and the result is subtracted from the original map. The purpose of this step is to remove any large-scale residual noise (i.e. on scales larger than the beam) not removed by the filtering applied during DIMM data reduction. The same smoothing operation and subtraction are applied to a Gaussian kernel of FWHM 14 arcsec (i.e. equal to the Airy disc radius at 850 μm). In the second and final step of matched filtering the background-subtracted map is convolved with this kernel.

We show the S2LXS *XMM*-LSS field matched filtered instrumental noise mosaic in Fig. 5. S2LXS did not re-observe areas covered in S2CLS, hence the absence of data in the region corresponding

Downloaded from academic.oup.com/mnras/article/520/3/3669/7009221 by guest on 23 October 2026

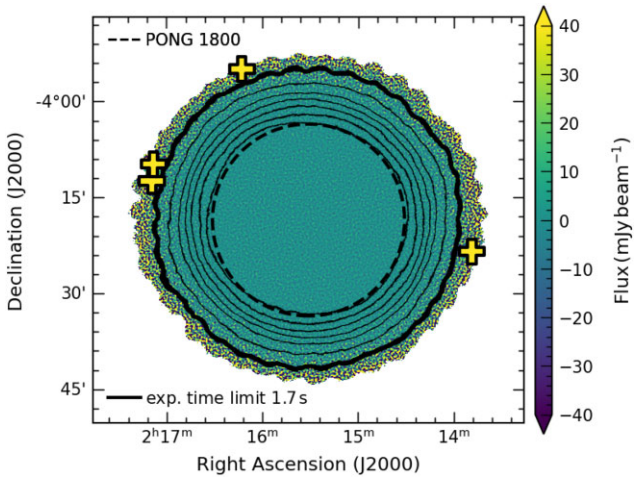


Figure 4. An example PONG tile (matched-filtered flux density map). The colour bar shows the flux density in mJy and the dashed circle shows the PONG map diameter of 1800 arcsec. Contours plotted in a thin black line are at 5–25 s in steps of 5 s, and illustrate how the exposure time decreases in the overscan region (outside the diameter of the PONG). The optimum exposure time cut of 1.7s is shown in the thick black line (see text for details of how this limit is derived and used). We also plot all $>5\sigma$ detections in this tile (crosses coloured with respect to the colour bar). All these (confirmed as spurious) detections lie in the overscan region of the PONG tile with flux densities $>$ 200 mJy. These erroneous detections highlight the need to apply a crop to the overscan region of the PONG tiles.

to the S2CLS UKIDSS-UDS field ($\alpha = 34.^\circ4542$, $\delta = -5.^\circ0986$). We overplot the footprints of CFHT CLAUDS (u^*), SWIRE mid-infrared (24 μm) and near-infrared (4.5 μm) imaging (Lonsdale et al. 2003), the HSC survey (Deep tier; Aihara et al. 2018), and the VISTA-VIDEO survey (Jarvis et al. 2013), highlighting the extent of multiwavelength coverage for the S2LXS *XMM*-LSS field. We note that the area of the S2LXS *XMM*-LSS field is fully encompassed by HerMES (Oliver et al. 2012), the HSC-Wide survey (Aihara et al. 2018), and *XMM*-LSS (Pierre et al. 2004), and so the footprints of these surveys are not plotted. The position of the 40 $> 5\sigma$ sources that make up the S2LXS *XMM*-LSS catalogue are also shown (see Section 3.2 for details of the catalogue).

2.3 Astrometric refinement and registration

During JCMT observations standard calibrators are regularly observed to identify and correct for drifts in the telescope pointing. Typical corrections are of the order of 1–2 arcsec. To refine the astrometry of the S2LXS *XMM*-LSS map, we require archival data from a survey which offers full coverage of the S2LXS *XMM*-LSS field. The HerMES and HSC-Wide survey both fully encompass the area of the S2LXS *XMM*-LSS science map. However, HSC-Wide is an optical survey and so samples a different population of galaxies compared to the population of dusty star-forming galaxies targeted in S2LXS *XMM*-LSS. In our tests (using the stacking method detailed below) with the HSC-Wide y-band data ($\lambda_{\rm eff} = 0.9762$ μm), we do not get an adequate signal-to-noise ratio in the final stack for a robust measurement of the offset in α and δ. Therefore, to refine the astrometry of our final science map we make use of the HerMES data, specifically the release 4 (DR4) xID250 catalogue. which comprises about 70 000 sources. Sources in the HerMES catalogue are blind detections at 250 μm with fluxes extracted in all *Herschel* Spectral and Photometric Imaging Receiver (SPIRE) bands (Roseboom et al. 2010, 2012; Oliver et al. 2012). We exclude sources that are detected at the edge of the *Herschel* SPIRE map, sources with $S_{250\,\mu{\rm m}} = 0$ and sources that fall outside the footprint of the S2LXS *XMM*-LSS mosaic, leaving us with a sample of approximately 30 000 sources. The individual PONG observations were taken over a prolonged period of 3 yr and so we would expect the drift in the telescope pointing to be different for individual PONG scans. However, there are not a sufficient number of HerMES sources within the footprint of each PONG tile to robustly measure the astrometry offset for each observation, noting that when we tested this using the individual PONG scans the uncertainties in the offsets derived were bigger than the offset values themselves. Therefore, our aim here is to identify and correct for any large-scale offset in the S2LXS *XMM*-LSS map. To do this we centre 100 arcsec × 100 arcsec cutouts of the S2LXS matched-filtered flux map at the positions of the HerMES sources and calculate the median value at each pixel position to create a median stack. We then use ASTROPY FIND_PEAKS (see Section 3.2 for details of this function) to measure the centroid position of the peak signal in the stack. The offset in α and δ is taken as the difference between the coordinates of the peak signal and the coordinates of the centre of the stack. We repeat this process several times, each time updating the world coordinate system reference pixel coordinates with the small changes in α and δ. The goal is to find the $\Delta\alpha$ and $\Delta\delta$ that maximize the signal-to-noise ratio of the stack in the central pixel and so this process is repeated until both $\Delta\alpha$ and $\Delta\delta$ converge. We measure offsets of $\Delta\alpha \simeq +0.84 \pm 0.17$ arcsec and $\Delta\delta \simeq -2.30 \pm 0.17$ arcsec which are comparable to the expected magnitude of the pointing drift. We apply these small systematic corrections to the S2LXS science maps.

3 ANALYSIS

3.1 Area coverage

In Fig. 5, we show the S2LXS *XMM*-LSS instrumental noise map which has a median 1σ depth of $1\sigma \simeq 4$ mJy beam^{-1}. The instrumental noise map is inhomogeneous, primarily due to (i) the variation in the median 1σ depth between the 42 PONG tiles that make up the S2LXS *XMM*-LSS map (see Section 2.2 for details of how the map was made), which ranges from 3.2 to 7.7 mJy beam^{-1} and (ii) the arrangement of the PONG tiles in an overlapping hexagonal pattern. The difference in the median 1σ depth of individual PONG tiles is largely driven by the number of PONG scans that are stacked to produce each PONG tile. The majority of the PONG tiles were observed over 5 PONG scans, however, due to the scheduling of observations 6 PONG tiles were observed more than 5 times, and so we have a larger number of PONG scans for these tiles (i.e. 6, 7, 10, 10, 18, 21 scans). The PONG tiles with additional scans are deeper (i.e. with 21 scans we reach a median 1σ depth of $1\sigma = 3.2$ mJy beam^{-1}) than the majority of PONG tiles that make up the map. The depth of the individual PONG tiles is also influenced by the weather conditions at the time of the observations and, in the case of one PONG tile (centred on $\alpha = 36.2566^\circ$, $\delta = -3.8432^\circ$) is due to one scan with only half the typical observation time (20 minutes). The instrumental noise across the S2LXS *XMM*-LSS map also varies depending on the number of overlapping PONG tiles. The median 1σ depth in the regions of the S2LXS *XMM*-LSS map with no overlapping PONG tiles is $1\sigma \simeq 5.9$ mJy beam^{-1}, compared to $1\sigma \simeq 4.3$ mJy beam^{-1} for regions with 2 overlapping tiles and $1\sigma \simeq 3.6$ mJy beam^{-1} for regions with $\geq$3 overlapping tiles. The instrumental noise also increases rapidly (to a maximum

Downloaded from academic.oup.com/mnras/article/520/3/3669/7009221 by guest on 23 October 2026

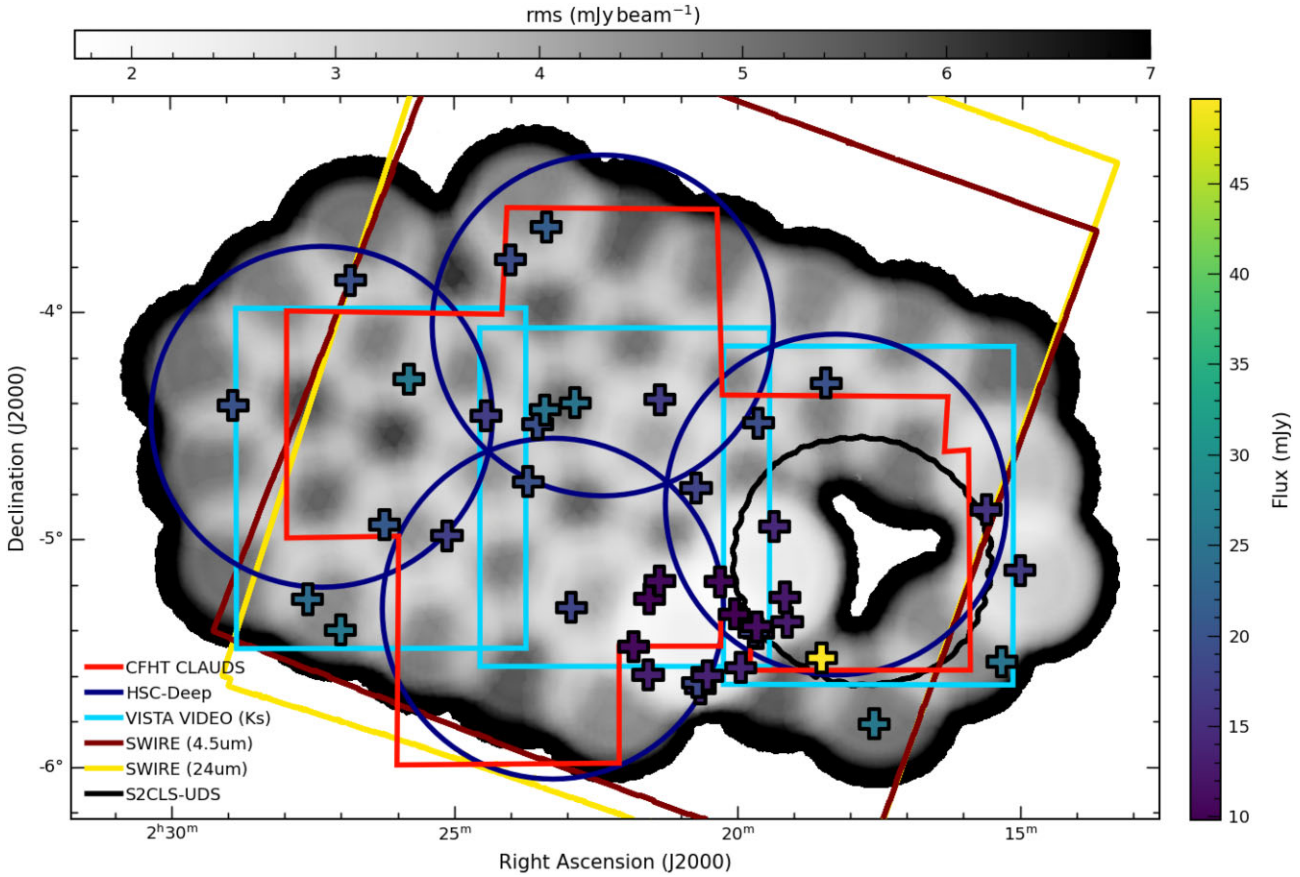


Figure 5. S2LXS *XMM*-LSS matched filtered instrumental noise map. The mosaic is made up of 42 hexagonally arranged PONG tiles which are cropped to an exposure time of 1.7 s. The colour map shows the 1σ depth in mJy beam^{-1} (horizontal colour bar). The S2LXS *XMM*-LSS map median rms is $1\sigma \simeq 4$ mJy beam^{-1}. The absence of data corresponds to the previously observed S2CLS UKIDSS-UDS field ($\alpha = 34\overset{\circ}{.}4542$, $\delta = -5\overset{\circ}{.}0986$ – black outline; Geach et al. 2017), which was not observed in S2LXS. We overplot the footprints of CFHT CLAUDS (u^*), the HSC-Deep survey (Aihara et al. 2018), the VISTA-VIDEO survey (Jarvis et al. 2013), and SWIRE 4.5 μm and 24 μm imaging (Lonsdale et al. 2003) to demonstrate the coverage of the multiwavelength data. The area of the S2LXS *XMM*-LSS field is fully encompassed by HerMES (Oliver et al. 2012), the HSC-Wide survey (Aihara et al. 2018), and *XMM*-LSS (Pierre et al. 2004), so the footprints of those surveys are not shown. The crosses in this figure indicate the positions of the $40 > 5\sigma$ sources detected in the S2LXS *XMM*-LSS field, coloured with respect to the observed flux (vertical colour bar). We note that whilst some of the S2LXS *XMM*-LSS sources appear to cluster (potentially tracing large-scale structure), the location of these sources is more likely a consequence of the variation in instrumental noise across the map, in part due to the overlap of the PONG tiles, with the majority of sources (67.5 per cent) detected in regions where at least 3 tiles overlap. This is not unexpected given that map is more sensitive ($1\sigma \simeq 3.6$ mJy beam^{-1}) in these overlap regions.

noise of $1\sigma_{\rm max} = 27.0$ mJy beam^{-1}) in the outer edges of the S2LXS *XMM*-LSS mosaic, where the overscan regions of individual PONG tiles do not overlap with neighbouring tiles. In Fig. 6, we show the cumulative area of the map as a function of depth highlighting the contribution due to the number of overlapping PONG tiles. The S2LXS *XMM*-LSS science map has an approximate area coverage of 9 deg^2.

The confusion limit ($\sigma_{\rm c}$; Scheuer 1957) is the flux level at which pixel-to-pixel variance (σ^2) ceases to reduce even with increased exposure time, due to the crowding of faint sources within the telescope beam. The confusion limit of an image is typically reached when the surface density of sources exceeds 0.03 per beam (e.g. Condon 1974; Hogg 2001). The confusion limit is measured in previous SCUBA-2 surveys and estimated to be $\sigma_{\rm c} \simeq 1$ mJy beam^{-1} at 850 μm (e.g. Geach et al. 2017; Simpson et al. 2019). With a median 1σ depth of $1\sigma \simeq 4$ mJy beam^{-1} the variance in our maps is dominated by instrumental noise (even in deeper overlap areas) and so we do not consider the sub-dominant effect of confusion noise on the S2LXS *XMM*-LSS survey any further.

3.2 Source extraction

The S2LXS *XMM*-LSS field has extensive multiwavelength coverage that might ordinarily encourage a prior-based source extraction approach. However, about 20 per cent of SMGs that are detected at 850 μm are undetected in sensitive near-infrared imaging at $K \gtrsim 25.7$ mag$_{\rm AB}$ (e.g. Dudzevičiūtė et al. 2019). To avoid overlooking this otherwise obscure minority of the SMG population we opt for a blind source extraction approach, in keeping with S2CLS (Geach et al. 2017) and S2COSMOS (Simpson et al. 2019). We caveat that a limitation of using a blind source extraction approach is that we will not separate out multiple discrete sources blended in the coarse 15 arcsec resolution of the SCUBA-2 beam (e.g. Simpson et al. 2015; Stach et al. 2018).

The S2LXS *XMM*-LSS maps have already been optimized for the detection of point source emission with the application of a matched-filter (see Section 2.2 for details). We use PHOTUTILS,[1] an ASTROPY

[1]In this work, we use ASTROPY version 4.2.1 and PHOTUTILS version 1.0.1.

Downloaded from academic.oup.com/mnras/article/520/3/3669/7009221 by guest on 23 October 2026

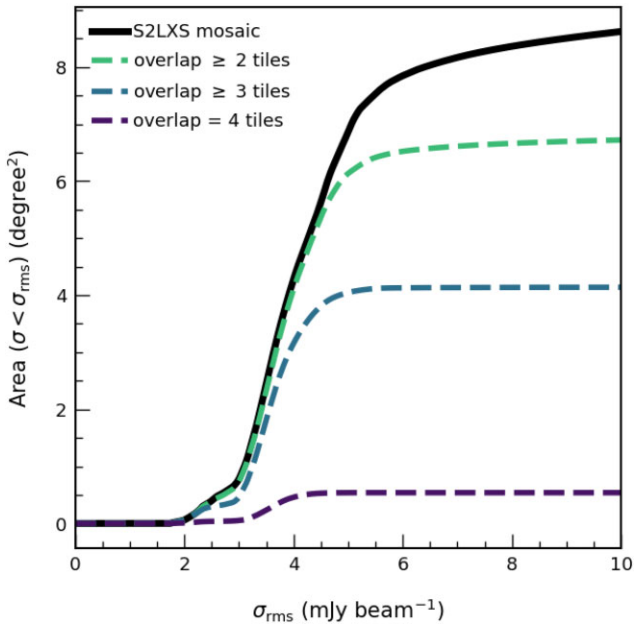


Figure 6. Cumulative area of the S2LXS *XMM*-LSS field mosaic as a function of instrumental noise (black solid line). We also show the cumulative area for regions of the map with ≥2, ≥3, and 4 overlapping PONG tiles, to highlight how the arrangement of the PONG tiles influences the depth of the S2LXS *XMM*-LSS map.

affiliated PYTHON package to detect sources in the S2LXS *XMM*-LSS signal-to-noise ratio matched-filtered map. This package includes a function FIND_PEAKS to locate local maxima in an astronomical image that are above a specified threshold value. We set a detection value of 3.5σ. Setting a low detection threshold allows us to explore the statistical properties of sources detected at the lowest significance in the S2LXS map, noting that it is simple to execute further cuts directly on the source catalogue. We also impose a separation limit, requiring sources to be separated by >15 arcsec (equivalent to the FWHM of the SCUBA-2 beam). If more than one source is detected above the detection threshold in a box size of 15 arcsec only the coordinates of the source with the highest signal-to-noise ratio are returned. This prevents double counting of bright sources if more than one pixel associated with a source exceeds the detection threshold. Whilst the bright-end of the 850 μm number counts is poorly constrained, these sources are expected to be rare (e.g. Cowley et al. 2015; Béthermin et al. 2017), with approximately 10 sources with flux densities above 10 mJy per square degree (e.g. Geach et al. 2017). Assuming sources are randomly distributed the probability of finding two 10 mJy sources separated by <15 arcsec is less than 0.1 per cent, so we are unlikely to overlook any bright sources by imposing this separation limit. However, we note that if bright sources are clustered (as seen at fainter fluxes e.g. Cairns et al. 2022; Greenslade et al. 2020) or are part of merging systems, imposing this separation limit may potentially exclude some sources. To mitigate this we can check for additional bright sources by visually inspecting the S2LXS *XMM*-LSS science map at the position of the sources in the survey catalogue, searching for elongated sources or clearly separated $>5\sigma$ signal-to-noise ratio peaks within the SCUBA-2 beam (noting that confirmation of multiple galaxies within the SCUBA-2 beam requires follow up by high-resolution interferometers). The FIND_PEAKS function allows the user to input a user-defined centroid function to calculate the coordinates of a source to sub-pixel accuracy. We create a function that calculates the centroid by fitting a model of the SCUBA-2 instrumental point spread function[2] (Dempsey et al. 2013) to the 2D distribution of the data. Using FIND_PEAKS and the parameters above we detect 1966 sources at $>3.5\sigma$ and 40 at $>5\sigma$. We inspect the S2LXS *XMM*-LSS images at the positions of sources in the $>5\sigma$ catalogue to check for multiple bright sources clustered within the SCUBA-2 beam, but find no evidence for this. The formal detection limit set for S2LXS *XMM*-LSS is 5σ and this is the threshold limit at which we define the survey catalogue. At this threshold, we estimate that the false detection rate is 10 per cent (see Section 3.7 for details). We note that whilst some of the S2LXS *XMM*-LSS sources appear to cluster (potentially tracing large-scale structure), the location of these sources in the S2LXS *XMM*-LSS map is more likely a consequence of the variation in instrumental noise across the map, in part due to the overlap of the PONG tiles, with the majority of sources (95 per cent) in the survey catalogue detected in deeper regions where ≥2 PONG tiles overlap.

3.3 Simulated SCUBA-2 maps

To test the reliability of our source extraction we create simulated SCUBA-2 maps projected on to the same pixel grid as the observed S2LXS *XMM*-LSS mosaic. To create our fake maps we must first produce a realistic instrumental noise map. We do this by creating a jack-knife map, which are typically produced by randomly inverting the flux densities for 50 per cent of the observed data before combining. This removes the astronomical signal from the stack and creates a realistic realisation of the instrumental noise. The S2LXS *XMM*-LSS mosaic is made up of 42 PONG tiles that are produced by stacking the ∼40 min PONG observations (i.e. the PONG scans, see Section 3 for details). For each PONG tile the simplest way to invert 50 per cent of the observed data is to invert the flux densities of half the PONG scans before combining. We do this for all PONG tiles composed of an even number of observations. However, the majority of the PONG tiles are observed over 5 scans and so for these tiles we cannot simply invert the flux densities of half the PONG scans. Therefore, for these PONG tiles, we randomly select one PONG scan and reduce the data (using the dimm reduction process and parameters described in Section 3) in two consecutive halves, producing two reduced maps each composed of 50 per cent of the data for the observation. For a PONG tile composed of 5 scans (for example), we can then invert 50 per cent of the observed data by inverting the flux densities of 2 randomly selected scans and of one of these 'split' scans (i.e. inverting the observed data for 2.5 scans).

To create a corresponding jack-knife tile for each PONG tile we invert the flux densities for 50 per cent of the observed data (as described above) and then combine with the remaining observations using the PICARD recipe MOSAIC_JCMT_IMAGES. To produce the jack-knife mosaic we then combine the 42 jack-knife tiles following the same method we used to create the S2LXS *XMM*-LSS mosaic (see section 2.2). In brief, we first apply a 1.7 s exposure time crop to each of the jack-knife tiles and then resample these individually to match the astrometric projection of the final science map. We then use inverse–variance weighting to combine the 42 re-sampled jack-knife tiles to produce the jack-knife mosaic. In Fig. 7, we compare the distribution of pixel values for the jack-knife signal-to-noise

[2]The SCUBA-2 PSF is well described by the superposition of two Gaussian functions: the primary component has an FWHM 13 arcsec and contains 98 per cent of the total flux; and the secondary component has an FWHM 48 arcsec and contains 2 per cent of the total flux (Dempsey et al. 2013).

Downloaded from academic.oup.com/mnras/article/520/3/3669/7009221 by guest on 23 October 2026

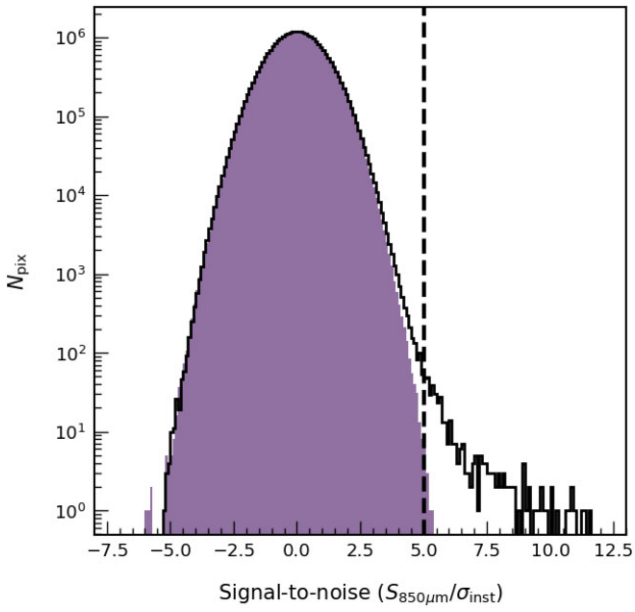


Figure 7. Distribution of pixel values in the matched-filtered signal-to-noise ratio jack-knife map (filled histogram). We also show the distribution of pixel values from the S2LXS *XMM*-LSS matched-filtered signal-to-noise ratio map (black stepped histogram) and the S2XLS *XMM*-LSS formal detection threshold of 5σ (black dashed line). This figure illustrates the characteristic tail of astronomical signal at positive fluxes. We also see a small number of pixel values with a signal-to-noise of <-5 in the jack-knife map. This is likely caused by isolated pixels with very low flux values in the sparsely sampled overscan regions of the PONG maps.

ratio matched-filtered mosaic to the distribution of pixel values in the S2LXS *XMM*-LSS signal-to-noise ratio map. We also show the S2LXS *XMM*-LSS $>5\sigma$ detection limit. This figure highlights the characteristic tail of astronomical signal, which is pronounced at $>5\sigma$.

The next step to create our simulated maps is to insert fake sources matching a realistic source count model into the jack-knife noise map. The faint end of the 850 μm number counts is well constrained and so we use the Schechter (1976) fit from Geach et al. (2017) to model the source counts below 15 mJy. However, the bright-end of the 850 μm number counts is not well constrained, with only 5 extragalactic sources in S2CLS with $S_{850\,\mu m} > 15$ mJy. Therefore, to model the source counts above 15 mJy we fit a simple power law to the S2LXS *XMM*-LSS observed number counts.

We simulate an observed SCUBA-2 source by convolving a point source of a given flux with the SCUBA-2 instrumental PSF (Dempsey et al. 2013), noting we impose a minimum flux limit of 1 mJy (in keeping with Geach et al. 2017). The simulated SCUBA-2 sources are then injected at random positions in the jack-knife noise map (we do not apply any conditions on the positioning of sources, these are inserted purely at random) to generate a simulated map. We then use the PICARD recipe SCUBA2_MATCHED_FILTER to apply a matched-filter to the simulated map and ASTROPY FIND_PEAKS to detect sources in the map above the floor detection threshold value ($>3.5\,\sigma$), mimicking the source extraction method used on the S2LXS *XMM*-LSS mosaic (see Section 3.2). A fake source is recovered if it is found above the detection threshold and at a maximum separation of 11 arcsec (0.75 × the FWHM of the SCUBA-2 beam) from the input coordinates. We note that this matching threshold is somewhat arbitrary, but is intentionally generous (and in keeping with the matching threshold used in Geach et al. 2017; Simpson et al. 2019). If there are multiple detections within this radius then the closest match is taken as the recovered source. If a source is recovered then the fake source catalogue will include the recovered flux density, rms, and coordinates of the source, as well as the signal-to-noise ratio of the detection. To allow us to fully sample the flux regime we are interested in (i.e. $S_{850\,\mu m} > 15$ mJy) we repeat this process 100 000 times, creating 100 000 simulated maps and corresponding fake source catalogues. For the source extraction on our simulated maps we use a floor detection limit of $>3.5\sigma$ to investigate the statistical properties of the simulated sources detected at low significance, and to compare to sources detected at the same threshold in the S2LXS *XMM*-LSS mosaic. However, for the remainder of this paper we assume the formal detection limit of S2LXS *XMM*-LSS which is 5σ.

3.4 Flux boosting

The flux density of galaxies detected at a relatively low signal-to-noise ratio is likely to be boosted upwards due to fluctuations in the noise (e.g. Hogg & Turner 1998). We can estimate the effect of flux boosting on the S2LXS *XMM*-LSS survey by comparing the recovered flux density to the intrinsic flux density for each source detected at $>5\sigma$ in the fake source catalogue. In Fig. 8, we show average flux boosting as a function of observed flux density and local instrumental noise, and as a function of signal-to-noise ratio. As expected the effect of flux boosting is most significant at a relatively low signal-to-noise ratio. At 5σ the observed flux density is approximately 66 per cent higher on average than the intrinsic flux density. We find that the relation between boosting ($\mathcal{B} = S_{obs}/S_{true}$) and signal-to-noise ratio is well described by a power law (equation 2). In keeping with Geach et al. (2017), we use a power law of the form $y = 1 + ax^k$, where a and k are constants, y = $\mathcal{B}$ and $x = (\mathrm{SNR}/5)$:

$$\mathcal{B} = 1 + 0.66\left(\frac{\mathrm{SNR}}{5}\right)^{-3.83} \quad (2)$$

In Fig. 8, we compare the average effect of flux boosting in S2LXS *XMM*-LSS to S2CLS (Geach et al. 2017), and find that the average effect of flux boosting is stronger in S2LXS *XMM*-LSS. We attribute this difference to the higher instrumental noise of the S2LXS *XMM*-LSS map.

Due to the statistical nature of flux boosting the intrinsic (true) flux density of a source with an observed flux density S_{obs} is drawn from a distribution $p\,(S_{true})$. We can empirically estimate the effect of flux boosting by measuring the histogram of injected flux densities of fake sources in bins of observed flux density and instrumental noise (see Fig. 9 for example). This empirical approach has been shown to be comparable (e.g. Geach et al. 2017) to traditional Bayesian techniques (e.g. Jauncey 1968; Coppin et al. 2005). To estimate the deboosted (true) flux density for each source in our $>5\sigma$ catalogue we draw 1000 samples from the $p\,(S_{true})$ distribution measured from our simulations for an observed flux density and local instrumental noise corresponding to that of the real source. We take the mean of the samples as the deboosted flux density of the real source and the standard deviation of the sample as the error on the deboosted flux density.

3.5 Completeness

We investigate the completeness of the S2LXS *XMM*-LSS survey by comparing the number of sources injected into the simulated

Downloaded from academic.oup.com/mnras/article/520/3/3669/7009221 by guest on 23 October 2026

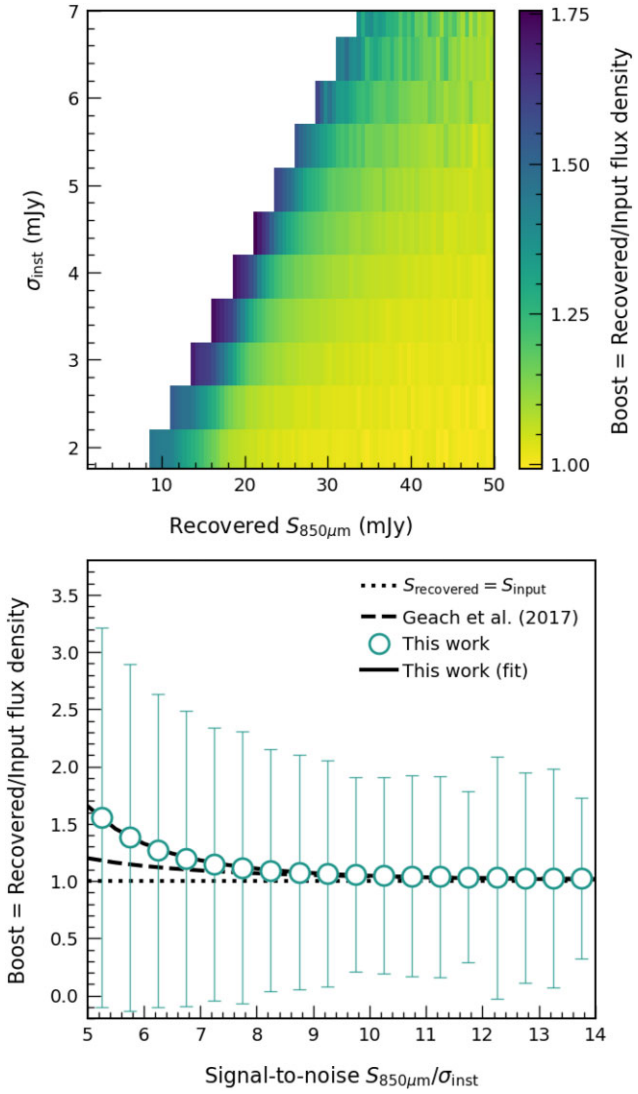


Figure 8. Flux boosting is measured by comparing the recovered flux density to the injected flux density for each source in the fake source catalogue. The top panel shows average flux boosting as a function of recovered (i.e. observed) flux density and local instrumental noise. In the bottom panel, we show average flux boosting (uncertainties shown as $\pm 1\sigma$) as a function of recovered signal-to-noise ratio (teal circles). We also plot the power-law relation from S2CLS (Geach et al. 2017, dashed curve) and the power-law fit from this work (solid curve, see equation 2). The dotted line shows $S_{\rm recovered} = S_{\rm input}$. The average effect of flux boosting is stronger in S2LXS *XMM*-LSS compared to S2CLS, which is likely motivated by the higher instrumental noise of the S2LXS *XMM*-LSS survey. As expected the effect of flux boosting is most significant for sources detected at relatively low signal-to-noise ratio.

SCUBA-2 maps to the number of sources recovered at $>5\sigma$, evaluated in bins of input flux density and local instrumental noise. In Fig. 10, we show the injected source counts and the estimated S2LXS *XMM*-LSS survey completeness as a function of input (true) flux density and local instrumental noise. The survey 50 per cent (90 per cent) completeness at the median map depth ($1\sigma \simeq 4$ mJy beam^{-1}) is 19.8 mJy (26.0 mJy). In Fig. 10, we plot the survey completeness across a range of map depths (2.0–6.5 mJy) to demonstrate the variation in survey completeness over the full survey area. Our binned completeness values act as a lookup table and we use 2D spline interpolation to estimate the completeness rate at the de-boosted flux density and local instrumental noise for each source in the S2LXS *XMM*-LSS $>5\sigma$ catalogue.

3.6 Positional uncertainty

Positional uncertainties are expected to scale with signal-to-noise ratio for a given Gaussian-like beam (Condon 1997; Ivison et al. 2007). We measure the positional offset ($\Delta\theta$) for each source in our fake catalogue by calculating the difference between the injected and recovered coordinates. In Fig. 11, we show the average positional offset as a function of signal-to-noise ratio for sources in the fake catalogue recovered at $>5\sigma$. We find that the relation is well described by a simple power law of the form

$$\Delta\theta = 2.17\,\mathrm{arcsec} \times \left(\frac{\mathrm{SNR}}{5}\right)^{-1.19}. \quad (3)$$

The average positional offset for sources detected at 5σ in S2LXS *XMM*-LSS is approximately 2 arcsec. This offset is consistent with theoretical predictions (e.g. equation B8 of Ivison et al. 2007), and the results of some SCUBA-2 wide-field surveys (e.g. Simpson et al. 2019; Shim et al. 2020). However, this is almost double the average positional uncertainty found in S2CLS (see Fig. 11), possibly due to S2CLS being a much deeper survey ($1\sigma \simeq 1$ mJy). The positional offset (equation 3) should be taken into account when identifying multiwavelength counterparts to sources in the S2LXS *XMM*-LSS $>5\sigma$ catalogue.

3.7 False detection rate

To estimate the false detection rate for the S2LXS *XMM*-LSS survey we compare the number of sources detected above a given threshold in the S2LXS *XMM*-LSS match-filtered signal-to-noise ratio map to the number of 'sources' (i.e. spurious detections) detected above the same threshold in the matched-filtered jack-knife map (see Section 3.3 for details of how the jack-knife map is created). In Fig. 12, we show the number of sources detected in the S2LXS *XMM*-LSS science map compared to the number of sources detected in the jack-knife map as a function of signal-to-noise ratio. We plot the purity rate (P) calculated as $P = (N_{\rm p} - N_{\rm n})/N_{\rm p}$, where $N_{\rm p}$ is the number of real + spurious sources detected above a given threshold in the S2LXS *XMM*-LSS mosaic and $N_{\rm n}$ is the number of jack-knife 'source' detections above the same limit. We find a false detection rate (purity rate) of 10.0 per cent (90.0 per cent) at $>5\sigma$ and 41.23 per cent (58.77 per cent) at $>4.5\sigma$.

As a check we repeat our analysis but instead of using the jack-knife map to estimate the number of spurious detections, we use the inverse of the S2LXS *XMM*-LSS match-filtered signal-to-noise map. The match-filtering process creates negative bowling around bright sources, and so we mask areas of negative bowling in the inverse map to avoid this contaminating our results. The estimated purity rate using this inverse method is comparable to that obtained using the jack-knife approach. We show the results from both methods in Fig. 12. In keeping with recent SCUBA-2 wide-field surveys (e.g. Geach et al. 2017; Simpson et al. 2019), we use the false detection rate estimates from the jack-knife approach for the remainder of this work. The S2LXS *XMM*-LSS survey formal detection threshold of $>5\sigma$ is chosen to give a 90 per cent purity rate. At this purity rate we expect ~4 of the 40 sources in the $>5\sigma$ catalogue to be spurious. We note that the false detection rate in S2XLS *XMM*-LSS is higher than expected at a detection threshold of 5σ (comparing to previous SCUBA-2 surveys, e.g. Geach et al. 2017; Simpson et al. 2019). This is possibly motivated by the steep slope of the 850 μm number

Downloaded from academic.oup.com/mnras/article/520/3/3669/7009221 by guest on 23 October 2026

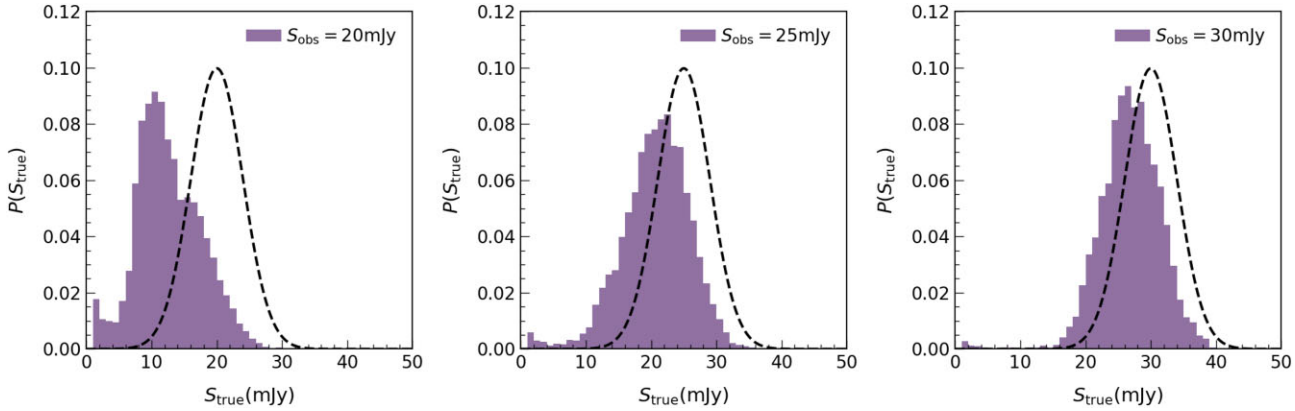


Figure 9. Distribution of injected (true) flux densities of sources in the fake source catalogue in bins of S_{obs} (shown in legend) and $\sigma_{inst} = 4$ mJy (approximately the 1σ median map depth). We also show a normal distribution centred on S_{obs} with a standard deviation of 4 mJy (dashed line). As expected for sources that are observationally bright (i.e. observed at higher signal-to-noise ratio with σ_{inst} fixed) the effect of flux boosting is diminished.

counts; at > 15 mJy there are very few real sources and so even a small number of spurious detections dramatically increases the false detection rate.

4 DISCUSSION

4.1 Bright-end number counts of the 850 μm population

In Table 2, we present the S2LXS *XMM*-LSS catalogue, which contains 40 sources with intrinsic flux densities in the range 7–48 mJy detected at a significance of $>5\sigma$. This catalogue includes observed and deboosted flux densities, completeness levels, positional uncertainties, and purity rates.

Number counts describe the surface density of sources per observed flux density interval (dN/dS), providing a simple measure of source abundance and a valuable tool to compare with model predictions. We estimate the 850 μm number counts for S2LXS *XMM*-LSS from the survey catalogue, correcting for the effects of flux boosting, incompleteness and the probability that an individual source is a false detection. We provide a brief description of this process here. For each of the 40 sources in the $>5\sigma$ catalogue (Table 2), we first estimate the deboosted (true) flux density by drawing a random sample from a $p(S_{true})$ distribution (estimated from our simulated maps, see Section 3.4 for details) consistent with the observed flux density and local instrumental noise of the source. We then apply a completeness correction, retrieving the completeness rate (which is estimated in bins of deboosted flux density and local instrumental noise) via 2D spline interpolation from the look up table generated in Section 3.5. Next we correct for the probability that a source is spurious based on the signal-to-noise ratio of the source detection (see Section 3.7). Once we have applied these corrections, we evaluate the corrected counts for the S2LXS *XMM*-LSS catalogue in flux intervals of $\Delta\log_{10}(S) = 0.1$, and then divide by the area of the S2LXS *XMM*-LSS science map[3] to measure the number counts (dN/dS) per flux interval per square degree. Since the observed flux density of a source maps on to a range of intrinsic flux densities, we evaluate dN/dS 1000 times (following the process above), each time randomly drawing the deboosted flux density for a source from the full intrinsic flux distribution ($p(S_{true})$). We take the final number counts as the mean of dN/dS across the 1000 realizations and the standard deviation of dN/dS in each flux bin as an additional uncertainty (to the Poisson error; Gehrels 1986). We note that the corrections for flux boosting and completeness are estimated in bins of flux density and instrumental noise to account for the variation in the instrumental noise in the S2LXS *XMM*-LSS mosaic.

The purpose of the various corrections we make is to recover the 'true' underlying source distribution. However, the simulations we use to derive the corrections are imperfect; i.e. the source count model we use at $S_{850\,\mu m} > 15$ mJy is based on the observed source counts of the S2LXS *XMM*-LSS survey. Therefore, it is important to test if any systematic biases remain. We also note that owing to the variation in instrumental noise across the S2LXS *XMM*-LSS mosaic we detect 95 per cent of sources in deeper regions of the map where at least 2 PONG tiles overlap, and so it is also crucial to test whether the location of sources detected in our map will influence ou r results.

To do this we inject a realistic source count model into our jack-knife map (see Section 3.3 for details of how the jack-knife map is created). The faint-end of the number counts is well constrained and so we use the Schechter (1976) fit from Geach et al. (2017) to model the source counts below 15 mJy. To produce a realistic number counts model above 15 mJy (noting that the bright-end of the 850 μm number counts is not well constrained in previous work) we fit a simple power law of the form $y = ax^k$ to the S2LXS *XMM*-LSS corrected number counts (see equation 4). We make an arbitary distinction between the 'faint' and 'bright' source count models at 15 mJy as this is consistent with the S2CLS results, which show an upturn in the 850 μm number counts above this flux density (Geach et al. 2017). We recover sources in an identical manner to the real data, adopting the formal detection threshold of the S2LXS *XMM*-LSS survey ($>5\sigma$). We then apply the various corrections (Sections 3.4, 3.5, and 3.7) to estimate the number counts. By comparing the recovered counts (before and after corrections) to the exact model counts injected into the maps we can test the effectiveness of our corrections. To check that our number counts corrections are not overly biased by the input source count model, we repeat the process above for two more extreme source count models (at the bright-end) by varying the slope k of the power law fit (in equation 4), using a model with a steeper slope $k = -6.60$ and a model with a shallower slope $k = -4.60$. We produce 100 simulated maps for each source

[3]To calculate the number counts per square degree we divide by the full area of the S2LXS *XMM*-LSS mosaic, as given the statistical nature of flux boosting a source in even the lowest flux bin could be found at any position in the S2LXS *XMM*-LSS mosaic.

Downloaded from academic.oup.com/mnras/article/520/3/3669/7009221 by guest on 23 October 2026

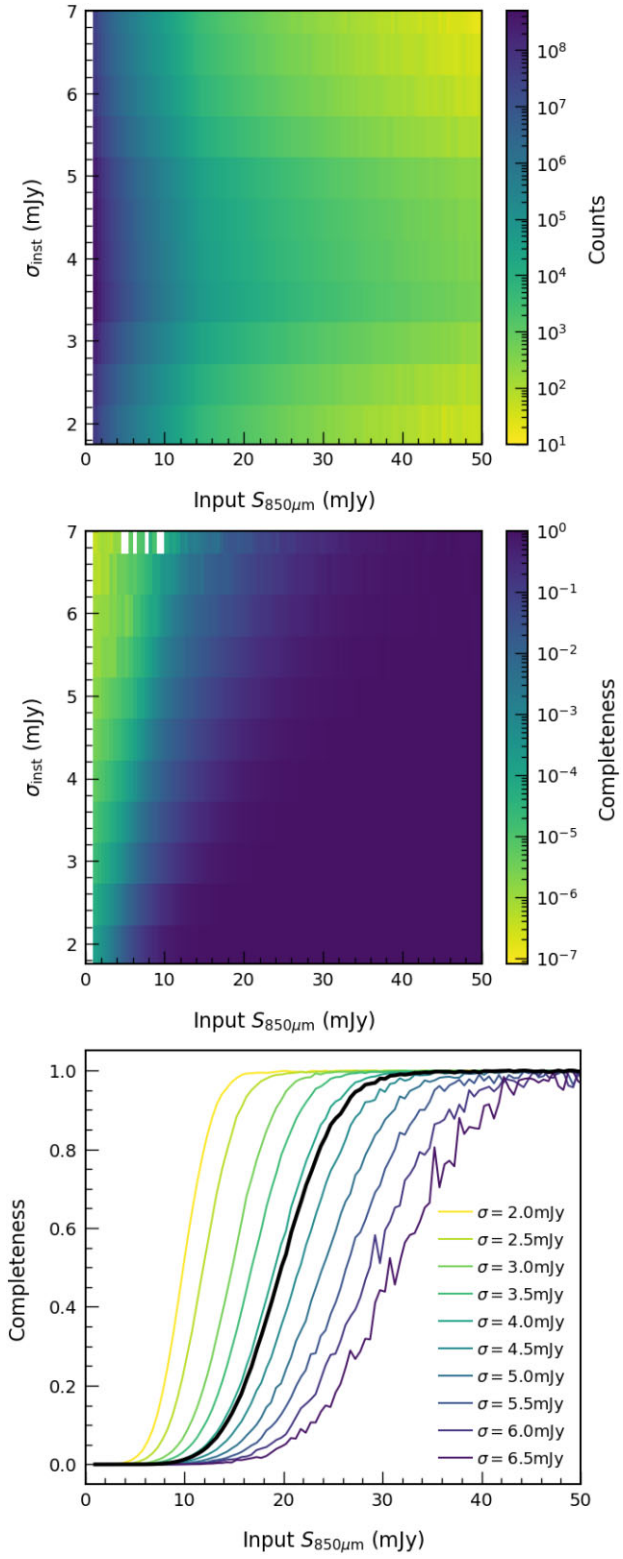


Figure 10. S2LXS *XMM*-LSS survey completeness estimated by comparing the number of sources injected into our fake maps to the number recovered at a detection threshold of 5σ. In the top panel, we show the injected fake source counts and in the centre panel the completeness ratio, both as a function of input flux density and local instrumental noise. In the bottom panel, we plot the survey completeness at the median map depth ($\sigma_{\rm inst} \simeq 4\,{\rm mJy\,beam^{-1}}$, black solid line) and at a range of map depths (see legend) to show the variation in completeness across the full S2LXS *XMM*-LSS survey area.

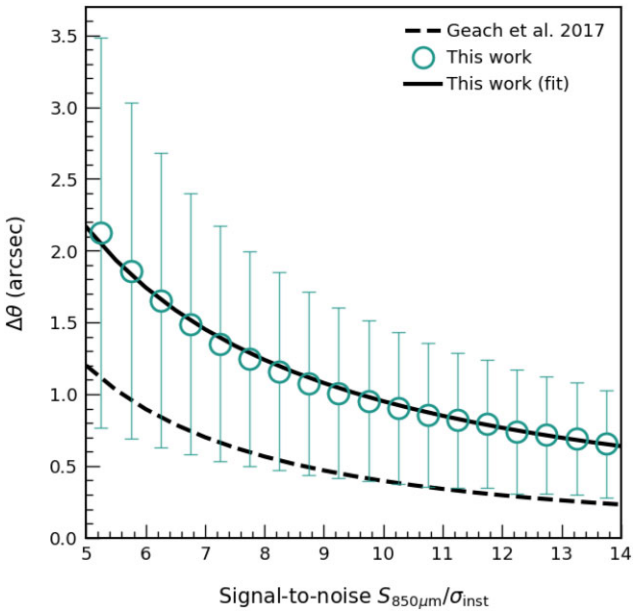


Figure 11. Positional offset ($\Delta\theta$) estimated by calculating the difference between the injected and recovered coordinates for each source in the fake catalogue. The average positional offset is shown (with $\pm 1\sigma$ uncertanties) as a function of signal-to-noise ratio (teal circles). We plot the power-law relation from Geach et al. (2017) (dashed line) and the power-law fit from this work (solid line, see equation 3). The positional offset is almost double the average positional uncertainty found in S2CLS, possibly due to S2CLS being a much deeper survey ($1\sigma \simeq 1$ mJy).

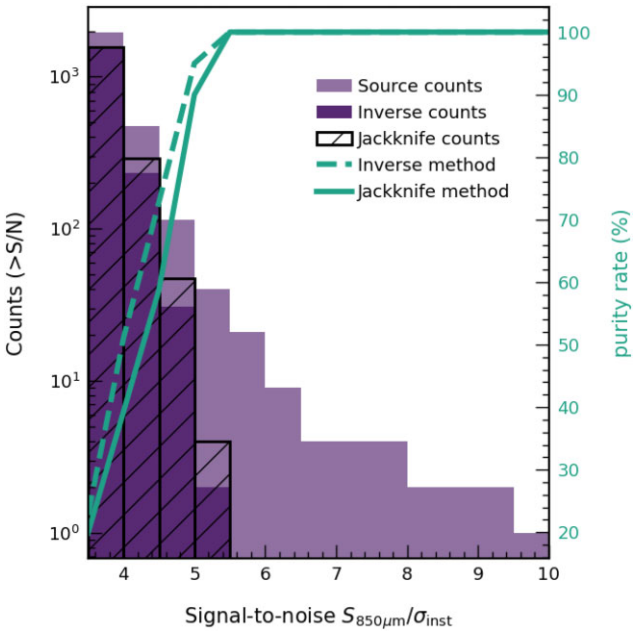


Figure 12. Purity rate estimated by comparing the number of sources in the S2XLS *XMM*-LSS science map to the number of spurious detections in the jack-knife map (solid line) above a signal-to-noise threshold. The purity rate is also estimated by comparing to the 'source' counts in the inverted S2XLS *XMM*-LSS science map (dashed line). We show the counts obtained from the S2XLS *XMM*-LSS science map (light purple), the inverse map (dark purple), and the jack-knife map (hatched histogram).

Downloaded from academic.oup.com/mnras/article/520/3/3669/7009221 by guest on 23 October 2026

Table 2. S2LXS *XMM*-LSS catalogue. This catalogue contains 40 sources detected at a significance of $>5\sigma$. Coordinates are J2000. The $S^{\rm obs}_{850\mu{\rm m}} \pm \sigma_{\rm inst}$ column gives the observed flux density and instrumental noise, the S/N column gives the signal-to-noise ratio of the detection, and the $S^{\rm deb}_{850\mu{\rm m}} \pm \sigma_{\rm tot}$ column gives the estimated deboosted (true) flux density and combined total (instrumental and deboosting) uncertainty. Column C gives the completeness level, $\Delta\theta$ the positional uncertainty (calculated from equation 3), and the final column P gives the purity rate.

S2LXS ID	RA	Dec.	$S^{\rm obs}_{850\mu{\rm m}} \pm \sigma_{\rm inst}$ (mJy)	S/N	$S^{\rm deb}_{850\mu{\rm m}} \pm \sigma_{\rm tot}$ (mJy)	C	$\Delta\theta$ (arcsec)	P
S2LXSJ021831−053131[a,d]	02 18 30.7	−05 31 31.3	49.7 ± 4.3	11.5	48.1 ± 6.3	1.00	0.80	1.00
S2LXSJ022700-052405	02 27 00.3	−05 24 05.2	26.0 ± 4.5	5.7	20.3 ± 7.4	0.37	1.85	1.00
S2LXSJ021735−054854	02 17 34.9	−05 48 53.6	25.9 ± 4.8	5.4	18.5 ± 7.9	0.19	1.99	0.97
S2LXSJ022548−041751[b]	02 25 47.7	−04 17 51.5	25.9 ± 3.3	7.7	23.1 ± 5.4	0.97	1.29	1.00
S2LXSJ021520−053222	02 15 19.9	−05 32 21.8	25.4 ± 4.6	5.5	18.4 ± 7.7	0.22	1.95	0.99
S2LXSJ022252−042412	02 22 51.8	−04 24 12.0	25.3 ± 4.9	5.2	16.8 ± 8.0	0.10	2.09	0.93
S2LXSJ022324−042602	02 23 23.8	−04 26 01.7	25.1 ± 4.7	5.4	17.9 ± 7.7	0.19	1.99	0.98
S2LXSJ022735−051558	02 27 35.2	−05 15 58.0	23.8 ± 4.1	5.9	18.6 ± 6.5	0.43	1.79	1.00
S2LXSJ022322−033747	02 23 22.1	−03 37 47.5	21.5 ± 4.1	5.3	14.1 ± 6.8	0.10	2.04	0.95
S2LXSJ022614−045616	02 26 13.7	−04 56 15.5	21.0 ± 3.7	5.6	15.2 ± 6.2	0.25	1.89	1.00
S2LXSJ022854−042445	02 28 54.0	−04 24 45.2	20.0 ± 3.6	5.6	13.8 ± 5.9	0.19	1.90	1.00
S2LXSJ021826−041900	02 18 26.4	−04 18 59.1	19.9 ± 3.8	5.2	13.1 ± 6.2	0.10	2.07	0.94
S2LXSJ022342−044501	02 23 41.8	−04 45 01.0	19.8 ± 3.5	5.7	14.0 ± 5.9	0.23	1.85	1.00
S2LXSJ022332−042948	02 23 31.5	−04 29 47.6	19.8 ± 3.9	5.1	12.7 ± 6.3	0.08	2.11	0.92
S2LXSJ022649−035146	02 26 49.3	−03 51 46.0	19.7 ± 3.4	5.8	14.1 ± 5.8	0.26	1.83	1.00
S2LXSJ021938−042930	02 19 37.9	−04 29 30.4	19.4 ± 3.1	6.3	14.9 ± 5.3	0.47	1.65	1.00
S2LXSJ022400−034623	02 24 00.3	−03 46 22.6	19.1 ± 3.4	5.6	13.4 ± 5.8	0.21	1.89	1.00
S2LXSJ022042-053806	02 20 42.0	−05 38 05.7	18.6 ± 2.4	7.9	16.4 ± 4.1	0.96	1.26	1.00
S2LXSJ021943−052436[c]	02 19 42.8	−05 24 35.8	18.4 ± 2.0	9.3	16.7 ± 3.7	0.99	1.03	1.00
S2LXSJ022256−051816	02 22 56.1	−05 18 15.6	17.9 ± 3.6	5.0	11.5 ± 5.5	0.07	2.16	0.90
S2LXSJ022044−044641	02 20 43.8	−04 46 40.8	17.8 ± 3.0	6.0	12.8 ± 5.2	0.28	1.74	1.00
S2LXSJ022508−045914	02 25 07.5	−04 59 13.7	17.4 ± 3.5	5.0	10.6 ± 5.3	0.05	2.16	0.91
S2LXSJ022122−042315	02 21 21.9	−04 23 15.1	17.0 ± 3.2	5.4	11.0 ± 5.1	0.11	1.98	0.98
S2LXSJ022426−042736	02 24 26.2	−04 27 36.1	17.0 ± 3.3	5.2	10.8 ± 5.1	0.08	2.07	0.94
S2LXSJ021501−050817	02 15 00.6	−05 08 16.6	16.8 ± 3.2	5.3	10.6 ± 5.1	0.08	2.04	0.95
S2LXSJ021536−045218	02 15 36.4	−04 52 17.9	15.9 ± 3.1	5.2	10.0 ± 4.8	0.07	2.08	0.94
S2LXSJ021921−045651[d]	02 19 20.9	−04 56 51.1	14.2 ± 2.3	6.1	10.3 ± 3.9	0.36	1.73	1.00
S2LXSJ022039−053937	02 20 39.3	−05 39 37.3	14.2 ± 2.6	5.5	9.5 ± 4.1	0.16	1.94	1.00
S2LXSJ021957−053406	02 19 56.5	−05 34 06.4	13.7 ± 2.5	5.6	9.4 ± 4.0	0.19	1.91	1.00
S2LXSJ022032−053615	02 20 31.7	−05 36 15.3	13.6 ± 2.3	5.8	9.6 ± 3.7	0.28	1.80	1.00
S2LXSJ021938−052502	02 19 37.9	−05 25 02.1	13.4 ± 2.1	6.5	9.9 ± 3.5	0.46	1.60	1.00
S2LXSJ022134−053558	02 21 34.5	−05 35 58.2	13.3 ± 2.3	5.7	9.3 ± 3.7	0.26	1.84	1.00
S2LXSJ021907−052202[d]	02 19 07.1	−05 22 01.6	12.7 ± 2.5	5.1	8.5 ± 3.9	0.10	2.14	0.91
S2LXSJ021910−051532[d]	02 19 09.8	−05 15 32.0	12.4 ± 2.4	5.1	8.4 ± 3.7	0.11	2.12	0.92
S2LXSJ021939−052315[d]	02 19 39.3	−05 23 15.0	11.1 ± 2.0	5.6	7.5 ± 3.1	0.15	1.89	1.00
S2LXSJ022122−051113	02 21 22.4	−05 11 13.0	11.0 ± 2.2	5.1	7.6 ± 3.3	0.12	2.14	0.91
S2LXSJ022018−051124	02 20 18.4	−05 11 23.9	10.9 ± 1.8	6.1	7.7 ± 3.0	0.18	1.72	1.00
S2LXSJ022150−052835	02 21 49.8	−05 28 34.6	10.8 ± 2.1	5.3	7.4 ± 3.1	0.13	2.03	0.96
S2LXSJ022133−051558	02 21 33.2	−05 15 57.5	10.4 ± 2.0	5.2	7.2 ± 3.1	0.12	2.09	0.93
S2LXSJ022003−052000	02 20 03.1	−05 19 59.5	9.8 ± 1.8	5.6	6.8 ± 2.9	0.09	1.91	1.00

[a]Ultrabright lensed submillimetre galaxy known as 'Orochi' (Ikarashi et al. 2011).
[b]Lensed hyperluminous infrared galaxy (HXMM05; Oliver et al. 2012; Bussmann et al. 2015).
[c]The SCUBA-2 source has five ALMA counterparts (Oliver et al. 2012; Bussmann et al. 2015).
[d]S2CLS UKIDSS-UDS source (Geach et al. 2017) with ALMA follow up observations (Stach et al. 2019).

count model, and take an average of the counts before and after the corrections.

In Fig. 13, we show the average $((\mathrm{d}N/\mathrm{d}S)_{\rm rec} - (\mathrm{d}N/\mathrm{d}S)_{\rm true})/(\mathrm{d}N/\mathrm{d}S)_{\rm true}$ before and after corrections have been applied for all three source count models. In the absence of corrections the number counts are underestimated by up to 99 per cent in the faintest flux bins ($S_{850\mu{\rm m}} \leq 18$ mJy), largely influenced by the incompleteness of the S2LXS *XMM*-LSS survey at these flux densities. For brighter flux bins, we generally see an overestimation of the number counts due to flux boosting. Once we apply corrections the right-hand panel of Fig. 13 shows that we can reliably recover the true source counts for all three source count models, noting that for the brightest flux bins $S_{850\mu{\rm m}} > 30$ mJy the corrections appear less effective, likely due to low number statistics (evidenced by the large Poisson errors).

The S2LXS *XMM*-LSS 850 μm differential and cumulative number counts are presented in Table 3 and Fig. 14. We show our results for intrinsic flux densities >7 mJy, with the minimum flux consistent with the deboosted flux density of the faintest source in the S2LXS *XMM*-LSS catalogue. Since the bright-end (>15 mJy) of the 850 μm differential number counts are no longer well represented by a Schechter (1976) function, we fit the S2LXS *XMM*-LSS 850 μm

Downloaded from academic.oup.com/mnras/article/520/3/3669/7009221 by guest on 23 October 2026

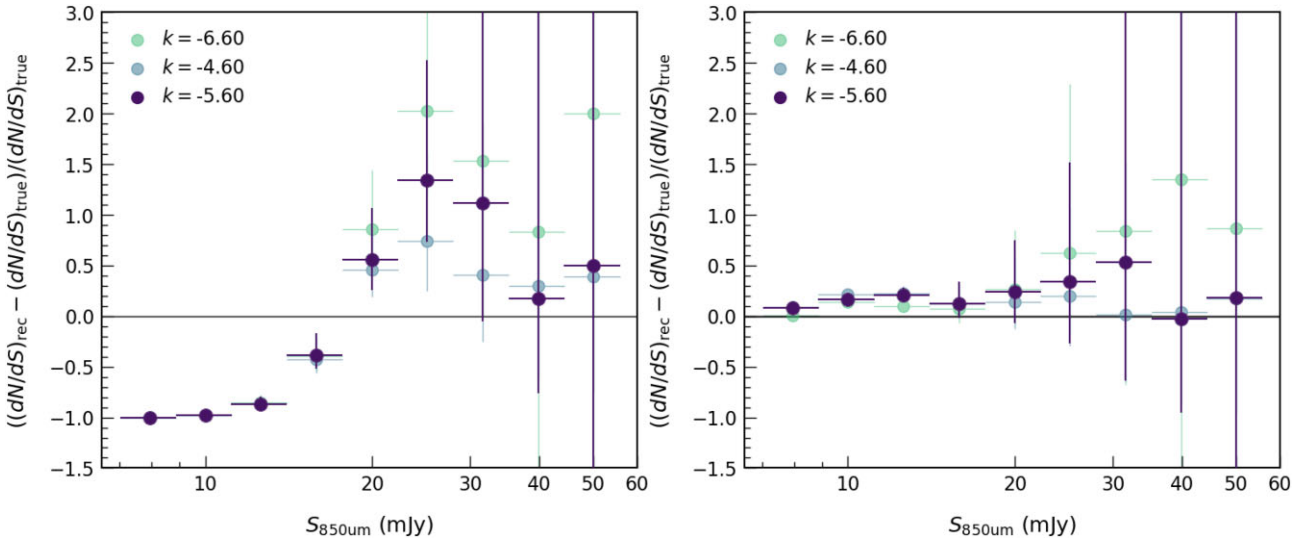


Figure 13. Comparison of recovered number counts to the 'true' number counts in simulated maps. We inject a realistic source count model into a jack-knife realization of the S2LXS *XMM*-LSS mosaic and then recover sources detected at $>5\sigma$ (the formal detection threshold of S2LXS *XMM*–LSS). To check that our number counts corrections are not overly biased by the input source count model we repeat this for two more extreme models by varying the slope k of the power law that we use to model the bright-end source count. In the left-hand panel, the recovered counts are not corrected for the effects of flux boosting, incompleteness or the probability that a source is a false detection. We show that in the absence of corrections the number counts are underestimated by up to 99 per cent in the faintest flux density bins ($S_{850\mu m} \leq 18$ mJy) in which incompleteness dominates. At brighter flux densities the number counts are generally overestimated due to flux boosting. In the right-hand panel, we show these counts with the various corrections applied, illustrating that the 'true' number counts can be robustly recovered. We note that in the brightest flux density bins ($S_{850\mu m} > 30$ mJy) the corrections are less effective, likely due to the low number statistics in these bins (evidenced by the large Poisson errors). The error bars in both panels show Poisson uncertainties (Gehrels 1986) only.

Table 3. Differential (dN/dS) and cumulative ($N > S'$) 850 μm number counts measured from the S2LXS *XMM*-LSS survey. We evaluate dN/dS 1000 times taking the mean as the final number counts estimate. The flux density bin widths are $\Delta\log_{10}(S) = 0.1$, with S and S' the flux bin centres and edges, respectively. The first set of errors shown are the Poisson uncertainties (Gehrels 1986) and the second set are the standard deviation on the number counts estimates over the 1000 realizations (see text for details).

$\log_{10}(S/\mathrm{mJy})$	S (mJy)	S' (mJy)	dN/dS (10^{-3} deg^{-2} mJy^{-1})	$N > S'$ (10^{-3} deg^{-2})
0.9	7.9	7.1	$18,637^{+203}_{-131} \pm 28,569$	$61,807^{+735}_{-618} \pm 53,964$
1.0	10.0	8.9	$7,762^{+179}_{-123} \pm 6,564$	$27,644^{+684}_{-566} \pm 14,965$
1.1	12.6	11.2	$2,221^{+138}_{-93} \pm 1,460$	$9,733^{+605}_{-485} \pm 4,056$
1.2	15.8	14.1	$525^{+103}_{-67} \pm 291$	$3,281^{+520}_{-398} \pm 981$
1.3	20.0	17.8	$204^{+79}_{-50} \pm 91$	$1,361^{+433}_{-306} \pm 403$
1.4	25.1	22.4	$47^{+50}_{-25} \pm 28$	$421^{+329}_{-191} \pm 165$
1.5	31.6	28.2	$6^{+30}_{-6} \pm 9$	$149^{+264}_{-111} \pm 64$
1.6	39.8	35.5	$2^{+23}_{-2} \pm 5$	$106^{+248}_{-88} \pm 13$
1.7	50.1	44.7	$7^{+21}_{-6} \pm 4$	$85^{+240}_{-75} \pm 44$

differential number counts (see Table 3 for values) with a power law (Fig. 14, solid black line):

$$\frac{\mathrm{d}N}{\mathrm{d}S} = (2.8 \pm 0.3) \times 10^6 \times \left(\frac{S_{850\mu m}}{\mathrm{mJy}}\right)^{-5.6\pm0.5}. \quad (4)$$

In Fig. 14, we also plot the observational constraints from S2CLS (Geach et al. 2017), S2COSMOS (Simpson et al. 2019) and the other main 850 μm wide-area surveys (e.g. Coppin et al. 2006; Weiß et al. 2009; Casey et al. 2013; Chen et al. 2013; Shim et al. 2020) for comparison. The results from S2XLS *XMM*-LSS are in good agreement with these previous surveys for the flux range probed. We note that since the S2LXS *XMM*-LSS survey has a contiguous survey area of 9 deg^2 cosmic variance will have a smaller affect on our number count estimates compared to previous work, with Simpson et al. (2019) finding no significant variation in the 850 μm number counts on scales of 0.5–3 deg^2.

Owing to a slight overlap in the S2LXS *XMM*-LSS and S2CLS UKIDSS-UDS maps these surveys have 5 sources in common. One of these sources is an ultrabright lensed galaxy ('Orochi'; Ikarashi et al. 2011); with a flux density of $S_{850\mu m} \simeq 50$ mJy this is the brightest extragalactic source detected in either survey. Geach et al. (2017) find an excess in the S2CLS differential number counts [i.e. above the Schechter (1976) function fit] at $S_{850\mu m} > 15$ mJy (see Fig. 14). We find a similar upturn in the S2LXS *XMM*-LSS differential number counts, but with a survey area of 9 deg^2 we detect double the number of $S_{850\mu m} > 15$ mJy extragalactic sources (with 11 sources detected at $>5\sigma$), and so we are able to reduce the Poisson errors on these

Downloaded from academic.oup.com/mnras/article/520/3/3669/7009221 by guest on 23 October 2026

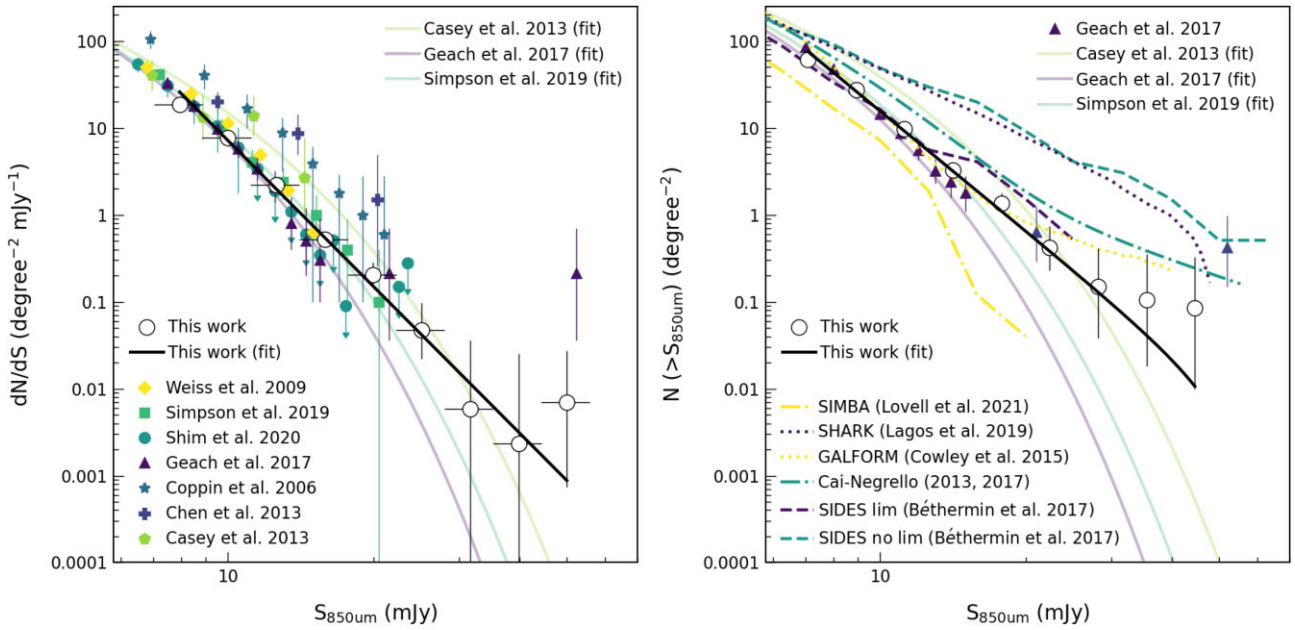


Figure 14. Number counts of 850 μm sources measured from the S2LXS *XMM*-LSS survey 5σ catalogue (white circles with black outline). In the left-hand panel, we present the differential number counts from this work along with observational constraints from S2CLS (Geach et al. 2017), S2COSMOS (Simpson et al. 2019), and the other main blank-field surveys (Coppin et al. 2006; Weiß et al. 2009; Casey et al. 2013; Shim et al. 2020), as well as from Chen et al. (2013) who combine data from two cluster lensing fields and three blank fields. The S2XLS *XMM*-LSS differential number counts are consistent with these previous studies within the uncertainties for the flux range probed. We find an excess in the number counts [above the Schechter (1976) function fit of Geach et al. (2017)] at $\gtrsim$15 mJy, similar to that found in S2CLS (Geach et al. 2017). In the right-hand panel, we present the S2LXS *XMM*-LSS cumulative number counts, comparing both to observations and several simulated galaxy models. For clarity, we only plot the observational constraints from S2LXS *XMM*-LSS and S2CLS, and the model fits from S2COSMOS and Casey et al. (2013). We show the 850 μm number counts from semi-analytical models (Cowley et al. 2015; Lagos et al. 2019), empirical models (Cai et al. 2013; Béthermin et al. 2017; Negrello et al. 2017) and the cosmological hydrodynamical simulation SIMBA (Lovell et al. 2021). The results from Lovell et al. (2021) and Cowley et al. (2015) both take into account blending from a 15-arcsec beam. The Béthermin et al. (2017) standard model has a star formation rate limit of 1000 $M_\odot$ yr^{-1}. We show the results both with and without this limit. The Béthermin et al. (2017) models shown do not take account of blending, but do include a prescription for lensing. The Cai–Negrello model combines the counts of unlensed and strongly lensed galaxies. The excess in the S2LXS *XMM*-LSS number counts at $\gtrsim$15 mJy is most consistent with the results from the Cai–Negrello empirical model (Cai et al. 2013; Negrello et al. 2017), the semi-analytical model of Cowley et al. (2015), and the standard empirical model of Béthermin et al. (2017). The error bars in both panels show Poisson uncertainties (Gehrels 1986).

measurements. The S2LXS *XMM*-LSS catalogue only includes one source with an observed flux density $S_{850\mu m} > 30$ mJy, and so our survey is hampered by low number statistics in this flux regime. This, coupled with our correction for the effects of flux boosting,[4] means we see large Poisson uncertainties on our number counts estimates at flux densities above 30 mJy.

An excess at the bright end of the number counts is also observed in studies at shorter (e.g. *Herschel* 500 μm; Negrello et al. 2010; Wardlow et al. 2013) and longer (e.g. South Pole Telescope 1.4 mm; Vieira et al. 2010; Mocanu et al. 2013) wavelengths, and is attributed to the presence of local objects and high-redshift gravitationally lensed sources (e.g. Negrello et al. 2010; Vieira et al. 2010). S2CLS provides tentative evidence that the over-abundance of sources at the bright-end of the 850 μm number counts is similarly influenced (Geach et al. 2017); of the three sources detected above 20 mJy in S2CLS the brightest ($S_{850\mu m} \simeq 200$ mJy) is a well-known Galactic object in the *Akari*-North Ecliptic Pole (the Cat's Eye Nebula) and another is a known ultra-bright lensed submillimetre galaxy ('Orochi' Ikarashi et al. 2011) which lies at $z_{phot} \simeq 3.5$, (Dudzevičiūtė et al. 2019). The S2XLS *XMM*-LSS >5σ catalogue includes at least two gravitationally lensed sources; 'Orochi' (Ikarashi et al. 2011) and a high-redshift ($z_{spec} \sim 3$) hyperluminous infrared galaxy from HerMES (Oliver et al. 2012; Bussmann et al. 2015; Leung et al. 2019). We visually inspect the available multiwavelength imaging (see Table 1) centred on the position of each S2LXS *XMM*-LSS source and query the NASA/IPAC Extragalactic Database (NED) for nearby $z < 0.1$ sources, allowing us to confirm that there are no Galactic objects in the S2LXS *XMM*-LSS catalogue. We also search the multiwavelength imaging and NED around the position of each S2LXS *XMM*-LSS source to identify bright, massive foreground galaxies, which are indicative of strong lensing. We find that for 16 (40 per cent) sources in the S2LXS *XMM*-LSS catalogue there is a bright, massive foreground galaxy within the SCUBA-2 beam. Whilst it is reasonable to expect (based on previous work) that the overabundance of sources observed at high flux densities in the S2LXS *XMM*-LSS survey is, at least in part, motivated by the presence high-redshift lensed galaxies, we cannot rule out a contribution from intrinsically bright sources (i.e. similar to GN20 a $S_{850\mu m} > 20$ mJy galaxy

[4]We evaluate dN/dS 1000 times each time randomly drawing the deboosted flux density for a source from a $p(S_{true})$ distribution (estimated from our simulated maps, see Section 3.4 for details) consistent with the observed flux density and local instrumental noise of the source. As we are sampling the full intrinsic flux distribution for a source, over the course of 1000 iterations, the estimated deboosted flux densities may map to more than one flux density bin. This is the reason we recover a number counts estimate for intrinsic flux densities 30 mJy $< S_{850\mu m} <$ 48 mJy despite no sources with observed flux densities in this range.

Downloaded from academic.oup.com/mnras/article/520/3/3669/7009221 by guest on 23 October 2026

detected in the SCUBA survey of the GOODS-North field; Pope et al. 2005; Daddi et al. 2009) or protocluster core type objects such as the Distant Red Core (DRC; Ivison et al. 2016; Oteo et al. 2018). It is also well known that a fraction of single dish 850 μm selected sources are the product of multiple fainter submillimetre galaxies that are blended in the coarse 15 arcsec resolution of the SCUBA-2 beam (e.g. Simpson et al. 2015; Stach et al. 2018). The multiplicity fraction increases with the brightness of the single dish source, with an estimated multiplicity fraction of 44 per cent for single dish 850 μm selected sources with flux densities $S_{850\mu m} > 9$ mJy (e.g. Stach et al. 2018). Surveys following up observations of single dish selected 850 μm sources with sub-arcsecond resolution interferometers find a systematic reduction in the estimated number counts by a factor of approximately 41 per cent at $S_{870\mu m} \geq 7$ mJy and 24–30 per cent at $S_{870\mu m} \geq 12$ mJy, though due to small number statistics the latter is not well constrained (e.g. Hill et al. 2018; Stach et al. 2018). We will explore the nature of the S2LXS *XMM*-LSS sources via follow up ALMA observations (Project ID: 2022.1.01030.S, PI: T. K. Garratt) of the brightest sources in the S2LXS *XMM*-LSS catalogue. With the exquisite resolution of ALMA we expect to pinpoint the position of multiwavelength counterparts to the brightest S2LXS *XMM*-LSS sources, allowing us to constrain the relative contributions of source blending, lensing, and intrinsically bright sources to the bright-end of the 850 μm number counts.

4.2 Comparison to models

In Fig. 14, we compare our results to: semi-analytical models GALFORM (Cowley et al. 2015; Lacey et al. 2016) and SHARK (Lagos et al. 2019); empirical models SIDES (Béthermin et al. 2017), and the Cai-Negrello model (Cai et al. 2013; Negrello et al. 2017); and the cosmological hydrodynamical simulation SIMBA (Lovell et al. 2021). These models are all able to broadly reproduce the faint-end of the 850 μm number counts (e.g. Geach et al. 2017; Simpson et al. 2019).

The blending of multiple faint submillimetre galaxies in the coarse 15 arcsec resolution of the SCUBA-2 beam is known to boost estimates of the 850 μm number counts, with follow up surveys (using sub-arcsecond resolution interferometers) finding a systematic reduction in the estimated number counts by a factor of approximately 41 per cent at $S_{870\mu m} \geq 7$ mJy. Of the models discussed here the semi-analytical model GALFORM, the empirical model SIDES and the hydrodynamical simulation SIMBA all simulate the effects of source blending in a 15 arcsec beam, which allows us to make a more 'like-for-like' comparison with the observed S2LXS *XMM*-LSS number counts. Lovell et al. (2021) use a 3D dust continuum radiative transfer code to estimate the submillimetre fluxes of galaxies in the cosmological hydrodynamic simulation SIMBA. To model the effects of source blending a projected SIMBA 850 μm light cone is convolved with the SCUBA-2 point spread function (Dempsey et al. 2013) to produce an 'observed' SCUBA-2 map. The SIMBA predicted 850 μm number counts are more than a factor of 2 below the observed S2LXS XMM-LSS counts. The semi-analytical model GALFORM (Lacey et al. 2016) invokes a mildly top-heavy initial mass function in starbursts to reproduce the observed number counts and redshift distribution (e.g. Wardlow et al. 2011; Simpson et al. 2014) of 850 μm selected sources (although we note this model is unable to reproduce the redshift distribution of bright SMGs with flux densities $S_{850\,\mu m} > 9$ mJy; Chen et al. 2022). Sources are extracted from the simulated maps using a top-down peak-finding approach and the number counts derived from the source-extracted catalogue. The GALFORM model is in good agreement with the observed S2XLS *XMM*-LSS counts within the uncertainties.

The upturn in the 850 μm number counts is motivated, at least in part, by the presence of high-redshift gravitationally lensed sources. A prescription for lensing is included in the empirical model of Béthermin et al. (2017), which uses an updated version of the two star-formation modes (Béthermin et al. 2012; Sargent et al. 2012) galaxy evolution model to derive global galaxy properties using empirical relations from observations. Taking the galaxy properties generated from this model, Béthermin et al. (2017) use an abundance matching technique to populate dark matter haloes with galaxies to produce a 2 deg^2 simulation of the extragalactic sky. The simulation includes a simple estimate of lensing that depends on redshift but does not account for the mass distributions in the foreground. Intrinsic number counts are estimated from the simulated catalogue. The standard model includes a sharp star formation limit of 1000 $M_\odot$ yr^{-1}. In Fig. 14, we plot the predicted intrinsic counts from Béthermin et al. (2017) for the standard model and the model with no star formation limit. We note that Béthermin et al. (2017) also estimate the number counts from a source-extracted catalogue to take into account source blending. The source-extracted counts mirror the intrinsic counts at bright flux densities and so for clarity we do not plot the source extracted counts in Fig. 14. The standard model is broadly in agreement with the S2LXS observed number counts below 30 mJy, but fails to reproduce the observed counts at higher flux densities. The model without a star-formation limit significantly overpredicts the counts by up to a factor 20 across the flux density range probed, which indicates that including a star formation limit in some form is necessary for this model to reproduce the observed counts. The Cai–Negrello empirical model (Cai et al. 2013; Negrello et al. 2017) also takes into account the influence of strongly lensed galaxy, by combining theoretical counts for late-type, unlensed and strongly lensed galaxies. The maximum magnification assumed for calculating the strongly lensed number counts is $\mu_{max} = 15$. We note that the Cai model (Cai et al. 2013) presented here has been re-calibrated in line with recent number counts measurements from Geach et al. (2017) and Simpson et al. (2019). The Cai–Negrello model overpredicts the S2LXS *XMM*-LSS observed number counts by a factor of approximately 2, apart from in the brightest flux bins where the counts are consistent within the uncertainties.

The semi-analytical model SHARK does not include a prescription for lensing or model the effects of source blending, and so, given these are known to be important influences, boosting the bright-end of the single-dish 850 μm, we might expect this model to underpredict the number counts compared to the observed S2LXS XMM-LSS counts. Lagos et al. (2019) combine the SHARK semi-analytical model (Lagos et al. 2018) with attentuation curves derived from EAGLE using the 3D dust radiative transfer code SKIRT (Trayford et al. 2017) to model the emission of galaxies from far-ultraviolet to far-infrared wavelengths. In Fig. 14, we show that the SHARK semi-analytical model overpredicts the bright-end of the number counts compared to the S2LXS *XMM*-LSS observed counts by up to a factor of 20.

The S2LXS *XMM*-LSS number counts are in broad agreement with the Cai–Negrello empirical model, the empirical model SIDES (at flux densities below 30 mJy) and the semi-analytical model GALFORM, which include gravitational lensing and/or the effects of source blending in a low-resolution single dish telescope beam, indicating that both may be important motivators for the observed overabundance of bright single dish selected 850 μm sources. With follow up ALMA observations (Project ID: 2022.1.01030.S) of the brightest sources in the S2LXS *XMM*-LSS catalogue we aim to place strong constraints on the contribution of instrinsically bright, lensed

Downloaded from academic.oup.com/mnras/article/520/3/3669/7009221 by guest on 23 October 2026

and blended sources to the bright-end of the 850 μm counts, vital to inform future models.

5 SUMMARY

We have presented the 850 μm maps and catalogue for the JCMT SCUBA-2 Large Extragalactic Survey of the *XMM*-LSS field. The S2LXS *XMM*-LSS survey maps a contiguous area of 9 deg^2 to a moderate depth of about 4 mJy beam^{-1}. This is the largest extragalactic area at 850 μm mapped with the JCMT to date. The wide area of the S2LXS *XMM*-LSS survey allows us to detect ultrabright ($S_{850\mu m} > 15$ mJy), but intrinsically rare sources, with approximately three sources expected per square degree with deboosted flux densities >15 mJy. The S2LXS XMM-LSS >5σ catalogue comprises 40 sources, of which 11 have deboosted fluxes above 15 mJy. This is twice the number of bright ($S_{850\mu m} > 15$ mJy) extragalactic sources detected in S2CLS. We use the S2LXS *XMM*-LSS >5σ catalogue to estimate the number counts at intrinsic flux densities above 7 mJy, significantly reducing the Poisson errors on existing measurements (e.g. Coppin et al. 2006; Chen et al. 2013; Geach et al. 2017; Simpson et al. 2019; Shim et al. 2020). We observe the distinctive upturn in the number counts that is expected to be caused by submillimetre emission from Galactic objects and gravitationally lensed high-redshift galaxies. We note that at least two sources in the S2LXS *XMM*-LSS 5σ catalogue are already known, lensed, high-redshift ($z \gtrsim 3$) galaxies (Bussmann et al. 2015; Geach et al. 2017). Follow-up ALMA observations (Project ID: 2022.1.01030.S, PI: T. K. Garratt) of the brightest sources in the S2LXS *XMM*-LSS catalogue will be a key step in unravelling the nature of the sources that contribute to the overabundance observed at the bright-end of the single dish 850 μm number counts. With the exquisite resolution of ALMA, we aim to constrain the relative contributions of source blending, lensing, and intrinsically bright sources to the bright-end of the 850 μm number counts; measure the redshift distribution for these rare, highly luminous galaxies; and explore whether a simple flux cut at 850 μm is an effective selection method to identify high-redshift, gravitationally lensed galaxies (Garratt et al. in preparation).

ACKNOWLEDGEMENTS

We thank Matthieu Béthermin, Claudia del P. Lagos, Zhen-Yi Cai and Mattia Negrello for providing their number counts. The James Clerk Maxwell Telescope is operated by the East Asian Observatory on behalf of The National Astronomical Observatory of Japan; Academia Sinica Institute of Astronomy and Astrophysics; the Korea Astronomy and Space Science Institute; the National Astronomical Research Institute of Thailand; Center for Astronomical Mega-Science (as well as the National Key R&D Program of China with No. 2017YFA0402700). Additional funding support is provided by the Science and Technology Facilities Council of the United Kingdom and participating universities and organizations in the United Kingdom and Canada. Additional funds for the construction of SCUBA-2 were provided by the Canada Foundation for Innovation. The data presented in this paper was taken as part of Program ID M17BL001. The authors wish to recognize and acknowledge the very significant cultural role and reverence that the summit of Maunakea has always had within the indigenous Hawaiian community. We are most fortunate to have the opportunity to conduct observations from this mountain.

TKG acknowledges support from a UK Science and Technology Facilities Council studentship. JEG is supported by a Royal Society University Research Fellowship. KEKC is supported by a Royal Society Leverhulme Senior Research Fellowship (SRF/R1/191013). KEKC and MF acknowledge support from the UK Science and Technology Facilities Council (grant number ST/R000905/1). CCC acknowledges support from the National Science and Technology Council of Taiwan (NSTC 109-2112-M-001-016-MY3 and 111-2112-M-001-045-MY3), as well as Academia Sinica through the Career Development Award (AS-CDA-112-M02). HD acknowledges financial support from the Agencia Estatal de Investigación del Ministerio de Ciencia e Innovación (AEI-MCINN) under grant (La evolución de los cíumulos de galaxias desde el amanecer hasta el mediodía cósmico) with reference (PID2019-105776GB-I00/DOI:10.13039/501100011033) and acknowledges support from the ACIISI, Consejería de Economía, Conocimiento y Empleo del Gobierno de Canarias and the European Regional Development Fund (ERDF) under grant with reference PROID2020010107. This work has been partially supported by the Japan Society for the Promotion of Science (JSPS) Grants-in-Aid for Scientific Research (19H05076 and 21H01128). This work has also been supported in part by the Sumitomo Foundation Fiscal 2018 Grant for Basic Science Research Projects (180923), and the Collaboration Funding of the Institute of Statistical Mathematics 'New Development of the Studies on Galaxy Evolution with a Method of Data Science'. MJM acknowledges the support of the National Science Centre, Poland through the SONATA BIS grant 2018/30/E/ST9/00208. HSH acknowledges the support by the National Research Foundation of Korea (NRF) grant, No. 2021R1A2C1094577, funded by the Korea government (MSIT). HS acknowledges the support from the National Research Foundation of Korea (NRF) grant, Nos. 2021R1A2C4002725 and 2022R1A4A3031306, funded by the Korea government (MSIT). YQX acknowledges support from the National Natural Science Foundation of China (NSFC) grants (12025303 and 11890693).

DATA AVAILABILITY

We release the S2LXS *XMM*-LSS >5σ catalogue as part of this publication, along with the 850 μm maps for use by the community. The data are available at the DOI https://doi.org/10.5281/zenodo.7371860 (European Organization For Nuclear Research OpenAIRE 2013).

REFERENCES

Aihara H. et al., 2018, PASJ, 70, S4
Alexander D. M., Bauer F. E., Chapman S. C., Smail I., Blain A. W., Brandt W. N., Ivison R. J., 2005, ApJ, 632, 736
Barger A. J., Cowie L. L., Sanders D. B., Fulton E., Taniguchi Y., Sato Y., Kawara K., Okuda H., 1998, Nature, 394, 248
Beichman C. A., Neugebauer G., Habing H. J., Clegg P. E., Chester T. J., 1988, in Infrared Astronomical Satellite (IRAS) Catalogs and Atlases. Volume 1: Explanatory Supplement. National Aeronautics and Space Administration, Washington DC
Bertin E., Mellier Y., Radovich M., Missonnier G., Didelon P., Morin B., 2002, in Bohlender D. A., Durand D., Handley T. H., eds, ASP Conf. Ser. Vol. 281, Astronomical Data Analysis Software and Systems XI. Astron. Soc. Pac., San Francisco, p. 228
Béthermin M. et al., 2012, ApJ, 757, L23
Béthermin M. et al., 2017, A&A, 607, A89
Boggess N. W. et al., 1992, ApJ, 397, 420
Bothwell M. S. et al., 2013, MNRAS, 429, 3047
Bussmann R. S. et al., 2015, ApJ, 812, 43
Cai Z.-Y. et al., 2013, ApJ, 768, 21

Downloaded from academic.oup.com/mnras/article/520/3/3669/7009221 by guest on 23 October 2026

Cairns J. et al., 2023, MNRAS, 519, 709
Casey C. M. et al., 2013, MNRAS, 436, 1919
Casey C. M., Narayanan D., Cooray A., 2014, Phys. Rep., 541, 45
Chapin E. L., Berry D. S., Gibb A. G., Jenness T., Scott D., Tilanus R. P. J., Economou F., Holland W. S., 2013, MNRAS, 430, 2545
Chapman S. C., Blain A. W., Smail I., Ivison R. J., 2005, ApJ, 622, 772
Chen C.-C. et al., 2016, ApJ, 820, 82
Chen C.-C. et al., 2022, ApJ, 929, 159
Chen C.-C., Cowie L. L., Barger A. J., Casey C. M., Lee N., Sanders D. B., Wang W.-H., Williams J. P., 2013, ApJ, 776, 131
Chen C.-T. J. et al., 2018, MNRAS, 478, 2132
Condon J. J., 1974, ApJ, 188, 279
Condon J. J., 1997, PASP, 109, 166
Coppin K. et al., 2006, MNRAS, 372, 1621
Coppin K., Halpern M., Scott D., Borys C., Chapman S., 2005, MNRAS, 357, 1022
Cowley W. I., Lacey C. G., Baugh C. M., Cole S., 2015, MNRAS, 446, 1784
da Cunha E. et al., 2015, ApJ, 806, 110
Daddi E. et al., 2009, ApJ, 694, 1517
Dempsey J. T. et al., 2013, MNRAS, 430, 2534
Dole H. et al., 2006, A&A, 451, 417
Dudzevičiūtė U. et al., 2020, MNRAS, 494, 3828
Eales S. et al., 2010, PASP, 122, 499
Eales S., Lilly S., Webb T., Dunne L., Gear W., Clements D., Yun M., 2000, AJ, 120, 2244
European Organization For Nuclear Research OpenAIRE, 2013, Zenodo, https://www.zenodo.org
Fixsen D. J., Dwek E., Mather J. C., Bennett C. L., Shafer R. A., 1998, ApJ, 508, 123
Frayer D. T., Ivison R. J., Scoville N. Z., Yun M., Evans A. S., Smail I., Blain A. W., Kneib J. P., 1998, ApJ, 506, L7
Geach J. E. et al., 2017, MNRAS, 465, 1789
Gehrels N., 1986, ApJ, 303, 336
Greenslade J., Clements D. L., Petitpas G., Asboth V., Conley A., Pérez-Fournon I., Riechers D., 2020, MNRAS, 496, 2315
Greve T. R. et al., 2005, MNRAS, 359, 1165
Hainline L. J., Blain A. W., Smail I., Alexander D. M., Armus L., Chapman S. C., Ivison R. J., 2011, ApJ, 740, 96
Hale C. L. et al., 2019, A&A, 622, A4
Hauser M. G. et al., 1998, ApJ, 508, 25
Hauser M. G., Dwek E., 2001, ARA&A, 39, 249
Heywood I. et al., 2022, MNRAS, 509, 2150
Heywood I., Hale C. L., Jarvis M. J., Makhathini S., Peters J. A., Sebokolodi M. L. L., Smirnov O. M., 2020, MNRAS, 496, 3469
Hill R. et al., 2018, MNRAS, 477, 2042
Hodge J. A., da Cunha E., 2020, R. Soc. Open Sci., 7, 200556
Hogg D. W., 2001, AJ, 121, 1207
Hogg D. W., Turner E. L., 1998, PASP, 110, 727
Holland W. S. et al., 1999, MNRAS, 303, 659
Holland W. S. et al., 2013, MNRAS, 430, 2513
Hughes D. H. et al., 1998, Nature, 394, 241
Ikarashi S. et al., 2011, MNRAS, 415, 3081
Ikarashi S. et al., 2015, ApJ, 810, 133
Ivison R. J. et al., 2007, MNRAS, 380, 199
Ivison R. J. et al., 2016, ApJ, 832, 78
Ivison R. J., Papadopoulos P. P., Smail I., Greve T. R., Thomson A. P., Xilouris E. M., Chapman S. C., 2011, MNRAS, 412, 1913
Jarvis M. et al., 2016, in MeerKAT Science: On the Pathway to the SKA. SISSA, Italy, p. 6
Jarvis M. J. et al., 2013, MNRAS, 428, 1281
Jauncey D. L., 1968, ApJ, 152, 647
Johnson S. P. et al., 2013, MNRAS, 431, 662
Kleinmann D. E., Low F. J., 1970, ApJ, 159, L165
Kreysa E. et al., 1998, in Phillips T. G., ed., Proc. SPIE Conf. Ser. Vol. 3357, Advanced Technology MMW, Radio, and Terahertz Telescopes. SPIE, Bellingham, p. 319
Lacey C. G. et al., 2016, MNRAS, 462, 3854
Lacy M. et al., 2021, MNRAS, 501, 892
Lagos C. d. P. et al., 2019, MNRAS, 489, 4196
Lagos C. d. P., Tobar R. J., Robotham A. S. G., Obreschkow D., Mitchell P. D., Power C., Elahi P. J., 2018, MNRAS, 481, 3573
Lawrence A. et al., 2007, MNRAS, 379, 1599
Leung T. K. D. et al., 2019, ApJ, 871, 85
Lonsdale C. J. et al., 2003, PASP, 115, 897
Lovell C. C., Geach J. E., Davé R., Narayanan D., Li Q., 2021, MNRAS, 502, 772
Low J., Kleinmann D. E., 1968, AJ, 73, 868
Magnelli B. et al., 2012, A&A, 539, A155
Mairs S. et al., 2021, AJ, 162, 191
Mauduit J. C. et al., 2012, PASP, 124, 714
Michałowski M. J. et al., 2017, MNRAS, 469, 492
Michałowski M. J., Dunlop J. S., Cirasuolo M., Hjorth J., Hayward C. C., Watson D., 2012, A&A, 541, A85
Miettinen O. et al., 2017, A&A, 606, A17
Mocanu L. M. et al., 2013, ApJ, 779, 61
Negrello M. et al., 2010, Science, 330, 800
Negrello M. et al., 2017, MNRAS, 465, 3558
Neugebauer G. et al., 1984, ApJ, 278, L1
Oliver S. J. et al., 2012, MNRAS, 424, 1614
Oteo I. et al., 2018, ApJ, 856, 72
Papovich C. et al., 2004, ApJS, 154, 70
Pierre M. et al., 2004, J. Cosmol. Astropart. Phys., 2004, 011
Pope A. et al., 2008, ApJ, 675, 1171
Pope A., Borys C., Scott D., Conselice C., Dickinson M., Mobasher B., 2005, MNRAS, 358, 149
Puget J.-L., Abergel A., Bernard J.-P., Boulanger F., Burton W. B., Desert F.-X., Hartmann D., 1996, A&A, 308, L5
Roseboom I. G. et al., 2010, MNRAS, 409, 48
Roseboom I. G. et al., 2012, MNRAS, 419, 2758
Sanders D. B., Mirabel I. F., 1996, ARA&A, 34, 749
Sargent M. T., Béthermin M., Daddi E., Elbaz D., 2012, ApJ, 747, L31
Sawicki M. et al., 2019, MNRAS, 489, 5202
Schechter P., 1976, ApJ, 203, 297
Scheuer P. A. G., 1957, Proceedings of the Cambridge Philosophical Society, 53, 764
Scott K. S. et al., 2008, MNRAS, 385, 2225
Scoville N. et al., 2007, ApJS, 172, 1
Shim H. et al., 2020, MNRAS, 498, 5065
Simpson J. M. et al., 2014, ApJ, 788, 125
Simpson J. M. et al., 2015, ApJ, 807, 128
Simpson J. M. et al., 2019, ApJ, 880, 43
Simpson J. M. et al., 2020, MNRAS, 495, 3409
Siringo G. et al., 2009, A&A, 497, 945
Smail I., Ivison R. J., Blain A. W., 1997, ApJ, 490, L5
Stach S. M. et al., 2018, ApJ, 860, 161
Stach S. M. et al., 2019, MNRAS, 487, 4648
Swinbank A. M. et al., 2014, MNRAS, 438, 1267
Swinbank A. M., Smail I., Chapman S. C., Blain A. W., Ivison R. J., Keel W. C., 2004, ApJ, 617, 64
Tacconi L. J. et al., 2006, ApJ, 640, 228
Thomson A. P. et al., 2012, MNRAS, 425, 2203
Trayford J. W. et al., 2017, MNRAS, 470, 771
Vieira J. D. et al., 2010, ApJ, 719, 763
Wang S. X. et al., 2013, ApJ, 778, 179
Wang W.-H. et al., 2017, ApJ, 850, 37
Wardlow J. L. et al., 2011, MNRAS, 415, 1479
Wardlow J. L. et al., 2013, ApJ, 762, 59
Weiß A. et al., 2009, ApJ, 707, 1201
Wilson G. W. et al., 2008, MNRAS, 386, 807

[1] *Centre for Astrophysics Research, University of Hertfordshire, Hatfield AL10 9AB, UK*
[2] *Division of Particle and Astrophysical Science, Nagoya University, Nagoya, Aichi 464-8602, Japan*

Downloaded from academic.oup.com/mnras/article/520/3/3669/7009221 by guest on 23 October 2026

[3]*Purple Mountain Observatory and Key Laboratory for Radio Astronomy, Chinese Academy of Sciences, 10 Yuanhua Road, Nanjing 210023, China*
[4]*School of Astronomy and Space Science, University of Science and Technology of China, Hefei 230026, Anhui, China*
[5]*Academia Sinica Institute of Astronomy and Astrophysics, No. 1, Section 4, Roosevelt Road, Taipei 10617, Taiwan*
[6]*Chinese Academy of Sciences South America Center for Astronomy, National Astronomical Observatories, CAS, Beijing 100101, China*
[7]*Imperial College London, Blackett Lab, Prince Consort Road, London SW7 2AZ, UK*
[8]*National Astronomical Observatories, Chinese Academy of Sciences, 20A Datun Road, Chaoyang District, Beijing 100101, China*
[9]*Instituto de Astrofísica de Canarias (IAC), E-38205 La Laguna, Tenerife, Spain*
[10]*Departamento de Astrofísica, Universidad de La Laguna, , E-38206 La Laguna, Tenerife, Spain*
[11]*National Space Institute, DTU Space, Technical University of Denmark, Elektrovej 327, DK-2800 Kgs. Lyngby, Denmark*
[12]*Department of Physics and Astronomy, University College London, Gower Street, London WC1E 6BT, UK*
[13]*Institute of Astronomy, Graduate School of Science, The University of Tokyo, 2-21-1 Osawa, Mitaka, Tokyo 181-0015, Japan*
[14]*Astronomy Program, Department of Physics and Astronomy, Seoul National University, 1 Gwanak-ro, Gwanak-gu, Seoul 08826, Republic of Korea*
[15]*SNU Astronomy Research Center, Astronomy Program, Seoul National University, 1 Gwanak-ro, Gwanak-gu, Seoul 08826, Republic of Korea*
[16]*Kavli Institute for Astronomy and Astrophysics, Peking University, No. 5 Yiheyuan Road, Haidian District, Beijing 100871, China*
[17]*Institute of Astronomy, Faculty of Physics, Astronomy and Informatics, Nicolaus Copernicus University, Grudziadzka 5, PL-87-100 Torun, Poland*
[18]*Astronomical Observatory Institute, Faculty of Physics, Adam Mickiewicz University, ul. Słoneczna 36, PL-60-286 Poznań, Poland*
[19]*Department of Astronomy and Physics, and Institute for Computational Astrophysics, Saint Mary's University, Halifax, NS B3H 3C3, Canada*
[20]*Department of Physics and Astronomy, University of British Columbia, Vancouver, BC V6T 1Z1, Canada*
[21]*Department of Earth Science Education, Kyungpook National University, Daegu 41566, Republic of Korea*
[22]*The Research Center for Statistical Machine Learning, the Institute of Statistical Mathematics, 10-3 Midori-cho, Tachikawa, Tokyo 190-8562, Japan*
[23]*CAS Key Laboratory for Research in Galaxies and Cosmology, Department of Astronomy, University of Science and Technology of China, Hefei 230026, China*
[24]*Department of Space, Earth and Environment, Chalmers University of Technology, Göteborg, 412 58, Sweden*

This paper has been typeset from a TEX/LATEX file prepared by the author.

Downloaded from academic.oup.com/mnras/article/520/3/3669/7009221 by guest on 23 October 2026